BRNO UNIVERSITY OF TECHNOLOGY

Faculty of Electrical Engineering
and Communication

MASTER'S THESIS

Brno, 2021 Bc. TATIANA PISARENKO

BRNO UNIVERSITY OF TECHNOLOGY
VYSOKÉ UČENÍ TECHNICKÉ V BRNĚ

FACULTY OF ELECTRICAL ENGINEERING AND COMMUNICATION
FAKULTA ELEKTROTECHNIKY A KOMUNIKAČNÍCH TECHNOLOGIÍ

DEPARTMENT OF ELECTRICAL POWER ENGINEERING
ÚSTAV ELEKTROENERGETIKY

CHARACTERIZATION OF PVDF MATERIAL IN NANOSCALE RESOLUTION
CHARAKTERIZACE VLASTNOSTÍ MATERIÁLU PVDF V NANOMĚŘÍTKU

MASTER'S THESIS
DIPLOMOVÁ PRÁCE

AUTHOR
AUTOR PRÁCE

Bc. Tatiana Pisarenko

ADVISOR
VEDOUCÍ PRÁCE

Mgr. Dinara Sobola, Ph.D.

BRNO 2021

BRNO UNIVERSITY OF TECHNOLOGY
FACULTY OF ELECTRICAL ENGINEERING AND COMMUNICATION

Master's Thesis

Master's study program **Electrical Manufacturing and Management**

Department of Electrical and Electronic Technology

Student: Bc. Tatiana Pisarenko ***ID:*** 177722

Year of study: 2 ***Academic year:*** 2020/21

TITLE OF THESIS:

Characterization of PVDF material in nanoscale resolution

INSTRUCTION:

Polyvinylidene fluoride nanofibers PVDF is a perspective material for sensors with excellent mechanical properties as flexibility, lightweight, chemical, and mechanical stability. Characterization of this material in nanoscale is essential for understanding processes responsible for the piezo effect and can provide additional knowledge for the enhancement of the performance of the material. Scanning probe microscopy SPM techniques provide a wide range of modes for characterization material piezoelectric properties with high resolution. Scan the individual nanofibers by scanning probe microscopy. On the basis of SPM, make conclusions regarding the piezoresponse of nanofibers in dependence on phase compositions of the samples. Study the morphology of the samples by SEM imaging and FIB cross-section. Provide characterization of the samples based on FTIR and Raman spectroscopy to determine phase composition.

RECOMMENDED LITERATURE:

[1] Scanning probe microscopy. New York, NY: Springer Berlin Heidelberg, 2015. ISBN 978-3-662-45239-4.

[2] SENGUPTA, D., A. G. P. KOTTAPALLI, S. H. CHEN, J. M. MIAO, C. Y. KWOK, M. S. TRIANTAFYLLOU, M. E. WARKIANI a M. ASADNIA. Characterization of single polyvinylidene fluoride (PVDF) nanofiber for flow sensing applications. AIP Advances. 2017, 7(10). DOI: 10.1063/1.4994968. ISSN 2158-3226. Dostupné také z: http://aip.scitation.org/doi/10.1063/1.4994968

Date of project specification: 8.2.2021 ***Deadline for submission:*** 24.5.2021

Supervisor: Mgr. Dinara Sobola, Ph.D.

doc. Ing. Petr Bača, Ph.D.
Chair of study program board

ABSTRACT

This work deals with the characterization of nanofibers based on polyvinylidene fluoride. The focus is on the piezoelectric properties of the fiber, which are studied by piezoelectric force microscopy. Thus, two types of different samples were measured, which differed in the fabrication parameters. The differences in the fibers in their phase composition were also investigated using Raman spectroscopy and Fourier-transform infrared spectroscopy. Chemical analysis of the surface and its state was performed using X-ray photoelectron spectroscopy. The different arrangement of the nanofibers together with their cross-section was observed by a scanning electron microscope using focused ion beam. The wettability and contact angle of the surface of the samples with demineralized water were also examined. It was found that the higher speed of the roller during the electrospinning process has a very significant effect on their arrangement and thus on the parameters affecting the formation of the piezoelectric effect and other material properties.

KEYWORDS

PVDF, PFM, electrospinning, nanofibers, STEM, FIB, Raman spectroscopy, FTIR

ABSTRAKT

Tato práce se zabývá charakterizací nanovláken na bázi polyvinylidenfluoridu. Zaměření práce je na piezoelektrické vlastnosti vlákna, které jsou studovány metodou piezoelektrické silové mikroskopie. Takto byly měřeny dva typy odlišných vzorků, které se lišily v parametrech výroby. Odlišnosti vláken v jejich fázovém složení byly také zkoumány za využití Ramanovy spektroskopie a infračervené spektroskopie s Fourierovou transformací. Chemická analýza povrchu a jeho stavu proběhla pomocí rentgenové fotoelektronové spektroskopie. Různé uspořádání nanovláken spolu s jejich průřezem bylo pozorováno rastrovacím elektronovým mikroskopem za využití fokusovaného iontového svazku. Rovněž byla zkoumána smáčivost a kontaktní úhel povrchu vzorků s demineralizovanou vodou. Bylo zjištěno, že vyšší rychlost otáček válce během procesu elektrostatického zvlákňování má velmi významný vliv na jejich uspořádání a tím i na parametry ovlivňující tvorbu piezoelektrického jevu a dalších materiálových vlastností.

KLÍČOVÁ SLOVA

PVDF, PFM, elektrostatické zvlákňování, nanovlákna, STEM, FIB, Ramananova spektroskopie, FTIR

ROZŠÍŘENÝ ABSTRAKT

Polyvinylidenfluorid (PVDF) je vysoce nereaktivní a čistý polymer, který se vyznačuje vysokou pevností a teplotní a chemickou odolností. Kromě velmi dobré inertní odolnosti má i výrazné piezoelektrické vlastnosti. Těmito vlastnostmi tak rozšiřuje svůj rozsah aplikace do mnohem širšího odvětví, a lze jej tak používat i jako elektrický nanogenerátor a harvester. Jako ideální využití pro PVDF se pak jeví například v textilním průmyslu, nositelné elektronice či v jiných aplikacích využívajících obnovitelné zdroje energie. Jedná se tak o poměrně perspektivní materiál pro mnoho využití. Za dosažením ideálních vlastností, konkrétně tedy vysokých hodnot piezoelektrického jevu a dalších parametrů jej ovlivňujících, však stojí komplexní množství proměnných, které mají vliv na vznik tohoto jevu. Jsou to zejména hodnoty volené již při výrobě PVDF. Jako ideální se jeví nanášení PVDF ve formě nanovláken. K tomu je zapotřebí takzvaného elektrostatického zvlákňování. Velmi osvědčená je metoda elektrospinningu, kdy jsou vlákna nanášeny na rotující válec vlivem elektrostatického napětí. Dobrým ukazatelem vysokých hodnot pro piezoelektrický jev u PVDF je pak β fáze. Vysoká β fáze byla zjištěna nejvíce při změnách rychlosti rotujícího kolektrorového válce. Jak se materiál chová při vysokých i nízkých otáčkách válce je tedy rozhodující vlastnost pro jeho výslednou funkci. Jeho charakterizace v rozsahu nanoměřítka se tak stává důležitou a žádanou pro možnosti dalšího vývoje a dosažení lepších výsledků pro konkrétní aplikace.

Tato práce charekterizuje PVDF nanovlákna na dvou odlišných rychlostech kolektorového válce. Vlákna byly nejdříve vyrobeny metodou elektrospiningu a poté zkoumány několika mikroskopickými a analytickými metodami, jako jsou například elektronová mikroskopie, mikroskopie atomárních sil v piezoresponzivním silovém režimu, Ramanova spektroskopie a další. Úspěšně vytvořená a charakterizovaná vlákna v této práci prokazují změnu několika jejich podstatných vlastností vlivem odlišných otáček kolektorového válce při výrobě. Tyto vlastnosti ovlivňují strukturu i elektrické parametry vlákna. Práce tak slouží jako důležitým a užitečným vodítkem pro další vědecké práce zabývající se výrobou PVDF nanovláken.

PISARENKO, Tatiana. *Characterization of PVDF material in nanoscale resolution*. Brno: Brno University of Technology, Faculty of Electrical Engineering and Communication, Department of Electrical Power Engineering, 2021, 54 p. Master's Thesis. Advised by Mgr. Dinara Sobola, Ph.D.

Author's Declaration

Author:	Bc. Tatiana Pisarenko
Author's ID:	177722
Paper type:	Master's Thesis
Academic year:	2020/21
Topic:	Characterization of PVDF material in nanoscale resolution

I declare that I have written this paper independently, under the guidance of the advisor and using exclusively the technical references and other sources of information cited in the paper and listed in the comprehensive bibliography at the end of the paper.

As the author, I furthermore declare that, with respect to the creation of this paper, I have not infringed any copyright or violated anyone's personal and/or ownership rights. In this context, I am fully aware of the consequences of breaking Regulation § 11 of the Copyright Act No. 121/2000 Coll. of the Czech Republic, as amended, and of any breach of rights related to intellectual property or introduced within amendments to relevant Acts such as the Intellectual Property Act or the Criminal Code, Act No. 40/2009 Coll. of the Czech Republic, Section 2, Head VI, Part 4.

Brno ....

author's signature*

*The author signs only in the printed version.

ACKNOWLEDGEMENT

I gratefully acknowledge my supervisor Mgr. Dinara Sobola, Ph.D., for professional guidance, advice, patience, and contributing ideas to work. I would like to extend my sincere thanks to doc. Ing. Klára Částková, Ph.D. that I was allowed to make nanofibers with her help.

Deepest gratitude belong to my parents, who have always stood by me and supported me even in the hard times. Without them, I wouldn't get so far.

Another persons who never wavered in their support were my closest friends, so I thank them too.

The creation of this work would not have been also possible without the support and nurture from my little bumblebee.

Research described in the paper was financially supported by the Grant Agency of Czech Republic under project No. 19-17457S, and by the Ministry of Education, Youth and Sports of the Czech Republic under the project CEITEC 2020 (LQ1601). Part of the work was carried out with the support of CEITEC Nano Research Infrastructure supported by MEYS CR (LM2018110).

Contents

List of Figures

Introduction

Piezoelectric materials are materials exhibiting a phenomenon of electrical polarization under mechanical stress. Therefore, mechanical energy is converted to electrical energy [1]. The advantage of piezoelectric polymers compared to piezoceramics is their high flexibility and easy processability [2]. Another advantage is their low toxicity and possible processing into nanostructures. Compared to piezoceramics, piezopolymers have orders of magnitude lower values of piezoelectric parameters [3].

In recent years, polyvinylidene fluoride (PVDF) has appeared to be a very promising material. It is a fluoropolymer with excellent chemical stability. The molecules of this polymer have a large dipole moment perpendicular to the polymer chain. Depending on the crystal structure, this leads to different electrical properties, which are used in many technical branches, such filters [4], and sensors [5].

For this reason, it is highly desirable to aim attention to this material and focus on its unique properties, especially for electrical use [6]. Studying the production and characterization and thus observing the sample's effects is essential for the formation of high-quality nanofibers.

Since these are fibers with the size of tens to hundreds of nanometers, their analysis and characterization become challenging. As a result, very fine techniques are needed that can examine samples within a single fiber. In addition, only one method is insufficient for a complete analysis of the influence of different parameters, so it is crucial to use several methods for reliable investigation and results [7]. One change of the fiber's parameter during fabrication does not have to affect only the phase changes of nanofibers but also the whole material. For example, their different arrangement may affect both the various piezoelectric properties within a single fiber and the strength, elasticity, or wettability of the entire sheet as a complete product [8].

1 Theoretical basis

This chapter covers a basic description of the study of PVDF nanofibers. Their properties were briefly described, especially the emphasis is on the description of the piezoelectric phenomenon, through the explanation of production methods to the possibility of fiber investigation. Given that the work focuses on the study of mainly the piezoelectric phenomenon depending on the properties of the fiber, such a description was chosen that would best suit the study of this problem.

1.1 Piezoelectric effect

The piezoelectric effect is the phenomenon in which the material is polarized by mechanical stress. Thus, mechanical energy is converted into electrical energy. The piezoelectric effect can be achieved with crystals that are not centrally symmetrical. Respectively, such crystals whose crystal lattice is formed by both positive and negative ions. These ions are always concentrated in one area. The phenomenon is reversible. As a consequence, the piezoelectric effect can be divided into direct and inverse. The inverse piezoelectric effect is also called electrostriction. This is basically the opposite of the direct piezoelectric effect. In the presence of an electric field, the crystals will be mechanically deformed. A relatively large electrical voltage is also required.

Piezoelectric materials can be both natural or artificial. Artificial materials include, for example, piezoceramics, which are composed of a large number of grains. Ceramic piezoelectric materials most often have a perovskite structure. During production, it must be exposed to intense polarization, which determines the orientation of mechanical stress and electric field [9].

1.1.1 Important piezoelectric constants

The electromechanical behavior of piezoelectric materials is described by several parameters that determine the properties. For each constant, two indexes are given according to the standard, which defines the directions of two corresponding values forming the constant.

Permittivity or dielectric constant is a material property, denoted ε, the unit is F/m, and indicates the amount of electrical induction inside the material caused by an external electric field of a certain intensity. The permittivity of the vacuum is denoted by ε_0 and has a value of $8.85 \times 10^{-12}\,\mathrm{F/m}$.

Piezoelectric charge coefficient indicates how many charges are generated under the action of mechanical stress and the amount of mechanical deformation under the action of this electric charge. Its denotation is d, and the unit is C/m. It can again have two lower indexes, the first index referring to the direction of polarization or electric field and the second index to the direction of mechanical stress or the direction of deformation. The coefficients d_{33}, d_{32}, and d_{15} are most often determined.

Dielectric dissipation factor or also the loss factor $\tan\delta$, without the unit, is the tangent of the angle of dielectric losses occurring during the phase shift of the current at alternating voltage.

Piezoelectric voltage coefficient is denoted as g and has the unit V m/N, and is also sometimes given as a pressure constant. It directly characterizes the piezoelectric phenomenon according to the induced electrical voltage on the sample with the unit dimension of the applied mechanical voltage.

1.2 Polyviniliedene fluorid

Polyvinylidene fluoride is a semi-crystalline polymer with high mechanical strength, thermal stability, good chemical resistance, and aging resistance. Compared to carbon and hydrogen, fluorine has a larger radius of the van der Waals effect, causing the dipole moment of the PVDF monomer. It also depends on the configuration of the homopolymer chain. PVDF exists in five phases: α, β, γ, δ and ϵ. The phases α and ϵ are non-polar, the remaining phases β, γ and δ are polar. Three of these phases illustrate Fig. 1.1. Thus, all polar phases exhibit piezoelectric properties, but most strongly β. The phases differ by the configuration of the chain, the difference between the phases α and β is usually presented in the literature as these phases are the most common as a result of electrospinning preparation procedure [10].

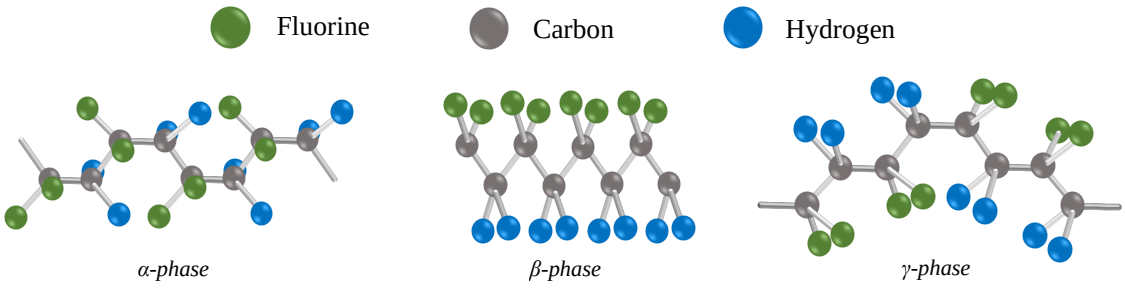

Fig. 1.1: Representation of the chain conformation for the alpha, beta and gamma phases.

1.3 Electrospinning

Electrospinning is one of the possibilities of nanofiber production. An electrostatic field is used here, where the polymer is charged with a high voltage. The collector is charged with the opposite polarity, or grounded and ”collects” this polymer. Due to the high voltage, the charge is transferred from the needle to the precursor and subsequently repelled, causing the drop to deform. According to the distance of the polymer solution and the collector, electrospinning can be divided into spinning with near-field electrospinning (NfeS) and spinning with far-field electrospinning (FfeS). These methods differ in the distance of the collector from the polymer dispenser. However, the main division of electrospinning is according to the method of ”dosing” the polymer. The result of the process is influenced both by the properties of the precursor, as well as by the set parameters and external conditions [11, 12].

As a highly utilized and efficient alternative method, which is often compared with electrospinning, is electrospraying. Allows deposition of nano or microparticles. Both of these methods use high voltage to promote the formation of nanomaterials. In the case of electrospraying, tiny droplets or particles are formed from a low viscosity solution. There is also electroblowing, a method that combines an electrostatic field with the forces of flowing gas.

1.3.1 Application with a metal rod

Electrostatic spinning from a metal rod uses a phenomenon in which a voltage is applied to the polymer. Nanofibers from the so-called Taylor cone are drawn due to the smallest resistance on the collector (Fig. 1.2), which is located at a sufficient distance so that all the solvent can evaporate from the nanofiber. The principle of the Taylor cone is based on the equilibrium state of a drop, which deforms into a conical shape, from which a stream of the polymer solution is then formed as a result of an increase in electrical voltage. The assembly consists of a high voltage source, a metal rod and a collector [13].

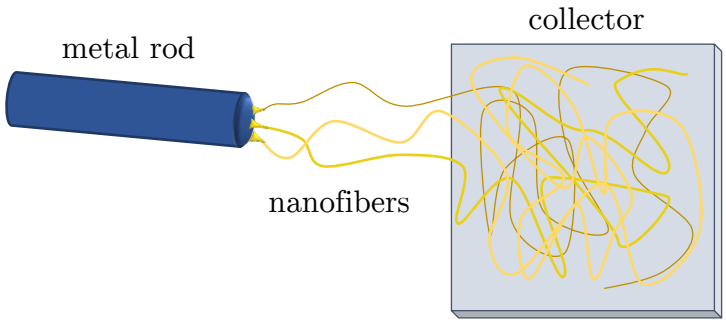

Fig. 1.2: Electrospinning with metal rod method.

1.3.2 Application with a syringe

It is also called nozzle electrospinning. A syringe terminated with a metal needle is used here as the "dispenser" of the polymer. A high voltage is applied to the needle, which charges the polymer solution. Alongside the needle tip, a collector is located at a certain distance, which is grounded or charged with the opposite polarity than the needle tip. When a voltage is applied to the polymer at the end of the needle, and due to the action of the electric field, a Taylor cone is formed at the end of the needle. At the end of the Taylor cone, a fiber is torn off, which is driven to a grounded or oppositely charged collector, on which it is captured (Fig. 1.3). In the first phase, the polymer solution contains about 80 to 90 % solvent, which further evaporates. In the second part of the process, the nanofiber is no longer visible, the "self-organization of the process" begins, and the drying and stretching of the nanofiber occur. Here, the material is applied in a spiral to the collector, on which it is attached. If we place the collector close to the syringe (i. e. closer than it is needed to evaporate the solvent), thicker fibers are formed that can stick together.

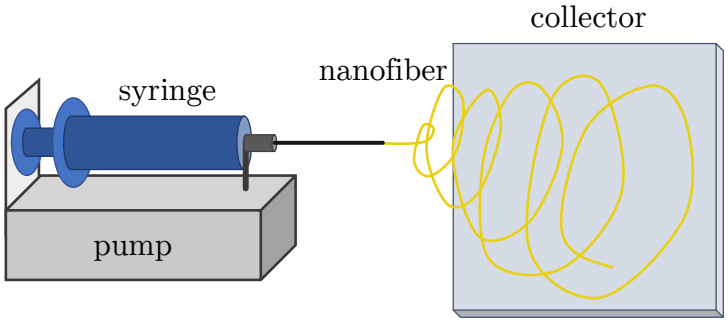

Fig. 1.3: Electrospinning with a syringe method.

1.3.3 Application with a rotating cylinder

The main difference from previous types of electrospinning is the absence of a capillary. The phenomenon of the formation of Taylor cones on a thin layer of the polymer solution is used here. The electrospinning process from the cylinder is based on the principle that the rotating cylinder, which is connected to a high voltage, is partially soaked in a polymer solution. In the upper position of the rotation of the cylinder, several Taylor cones are formed, from which the nanofibers can then be pulled out and subsequently collected on the collector (Fig. 1.4). The advantage of such a nanofiber production process is the possibility of forming very thin nanofiber layers [14].

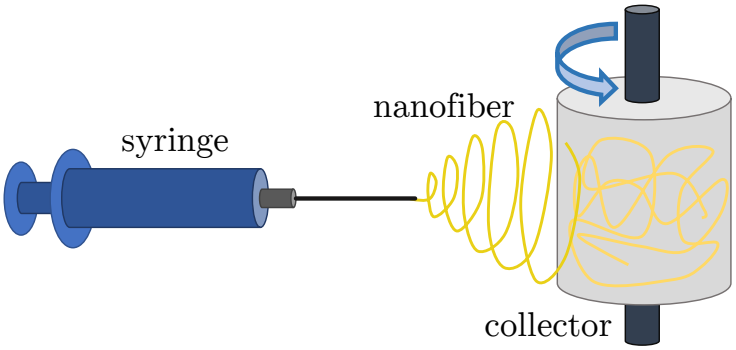

Fig. 1.4: Electrospinning with a rotating cylinder.

1.4 Selected methods for analysis and investigation of nanofibers

Numerous microscopic and analytical methods can characterize PVDF. Within the assignment of the diploma thesis, several most suitable methods were selected and described their basic principles, which allow the necessary structural, electrical and material characterization as effectively as possible.

1.4.1 Piezoresponse force microscopy (PFM)

Piezoresponse force microscopy (PFM) falls under scanning probe microscopy (SPM). The basis is the same as in atomic force microscopy (AFM), so it is an electrical modification. It is based on sensing the position of a small tip that moves along the surface of the sample in a raster. The sensitivity of the measurement is significantly dependent on the tip used, but under normal conditions, the lateral resolution is in the order of 10 nm, and the sensitivity in the z-axis is in sub-nanometres. The PFM is a non-destructive method, uses a contact mode, where the tip deflection is kept constant, and the feedback system copies the surface. If we plot the dependence of the force between the tip and the surface on their mutual distances, we could notice attractive forces (at greater distances, such as electrostatic or van der Waals forces) and repulsive forces (at smaller distances, due to the overlap of electron clouds). The tip copying the surface of the sample is conductive, and bias is applied to it as showed in Fig. 1.5. Tungsten, platinum, gold and diamond, and other conductive materials are used as coatings.

In this way, topographic and ferroelectric domains can be displayed simultaneously with high resolution. Ferroelectric materials have both pyroelectric and

piezoelectric properties. The ferroelectric domain is a spontaneous region of two polarization points in one direction. The other two neighboring domains are separated by a boundary wall, the nature of which is still unclear.

PFM can also characterize electrical properties, such as capacitance, electrostatic forces, operating functions, electric current [15].

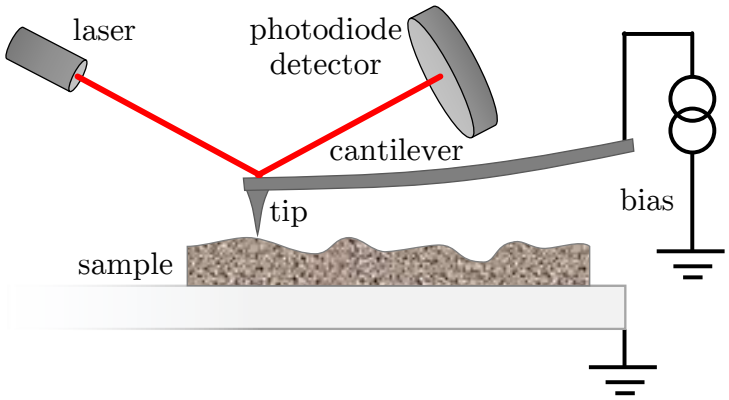

Fig. 1.5: Scheme of basic function of PFM.

1.4.2 Scanning electron microscopy (SEM)

Unlike conventional light microscopes, the scanning electron microscope (SEM) uses electrons instead of photons and electromagnetic lenses instead of glass lenses as the radiation source. In the entire internal space of the microscope, both the electron beam itself and the sample, are in a vacuum to prevent the electrons from interacting with the external atmosphere. The specimen observed in the SEM should be conductive, so to watch non-conductive materials, the sample can be pre-coated with a layer of metal powder (so-called sputtering).

Primary electrons impact the observed specimen and, by interacting with the mass, atomic electrons are driven from the sample. These atomic electrons are dragged to detectors by a suitable potential, which produces a signal modified for processing in an imaging system. The imaging system may be a screen on which an appropriate image is created by scanning an electron beam over the scanned area. The resulting image is an image that captures the surface structure of the specimen.

The standard accelerating voltage range for scanning electron microscopes is from tenths of kilovolts to tens of kilovolts. The electron beam current from pico ampere units to tens of nano ampere.

For the study or analysis of the surface, I use the interaction of the electron beam with the sample, which provides a wide range of information, whether the microstructure, crystallographic arrangement or chemical composition of the material. This information can be identified by the various signals emitted from the

sample, as illustrated in Fig. 1.6. To obtain them, the microscope must be equipped with detectors that collect this information [16]. The most commonly used is the secondary electron detector (SE), followed by the energy-dispersive X-ray (EDX) detector or the scanning transmission electron microscopy (STEM) detector.

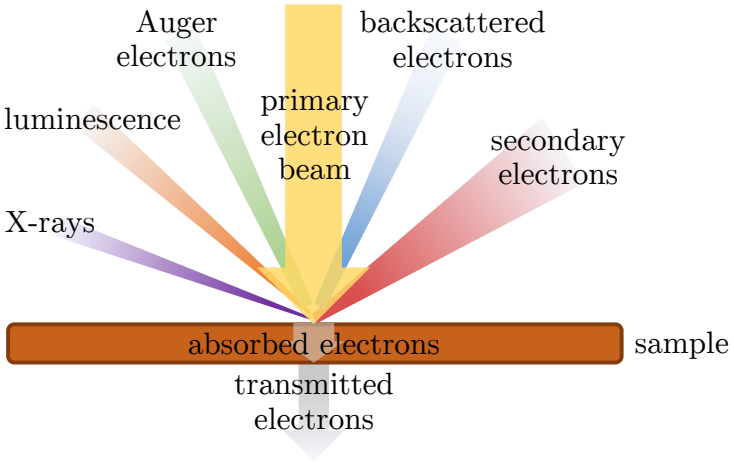

Fig. 1.6: Types of interactions between electrons and a sample.

Focused ion beam

Like an electron microscope, ions are a source of charged particles. These, mostly heavier, particles with high kinetic energy are also formed into a beam by a system of lenses and concentrated in a very small area. We can deflect the ion beam and perform rasterization. In addition to dedusting and deposition, the surface of the studied sample can also be imaged by detecting secondary ions, similar to using an electron beam.

Nowadays, it is possible to encounter many types of FIB microscopes, which differ both in the type of ions used and their acquisition and in the range of the accelerating voltage or the whole structure. Some types of microscopes, such as Xe plasma FIB, obtain ions from the plasma. It is also possible to use GFIS (gas field ion source), which means ionization of gas by a strong electric field. Currently, the most common types of FIB sources are liquid metal ion sources (LMIS), which produces a focused ion beam, in the source of which atoms of pure metal or its alloys in the liquid phase are ionized. For ionization in LMIS sources, Ga, In, Sn, i.e., are used with a low melting point. The FIB device with this source is also used in the context of this work, so it is subsequently given more attention.

A special type of SEM microscopes is double-beam microscopes, which in addition to the primary electron beam also have a focused ion beam (FIB), and are referred to as SEM-FIB microscopes. Thanks to the directed flow of ionized atoms,

this arrangement enables micro-cutting of the observed samples, which is suitable not only for the preparation of lamellae for transmission electron microscopy but also for so-called in situ experiments if the microscope is equipped with a nanoindenter.

1.4.3 Scanning transmission electron microscopy (STEM)

STEM combines the principle of both SEM and TEM. In contrast to the TEM, the scanning electron beam is deflected here and scans the sample. STEM works with a much lower accelerating voltage compared to TEM, which reaches up to 300 kV. STEM is an excellent technique for monitoring nanostructures and critical dimension measurements. The electrons pass through the sample and are detected on at least one detector located below it, as indicated in Fig. 1.7. Imaging can be performed with the following detectors:

- *bright field (BF)* is located in the center of the cone of illumination, where there is a minimal deflection of electrons, and they fall directly perpendicularly from the sample to the center of the detector;
- *dark field (DF)* where scattered electron are collected around the main beam;
- *high-angle annular dark-field (HAADF)* collects electrons by very high angle, also referred to as Rutherford scattered electrons [17].

STEM imaging can be performed either with a complete dedicated STEM microscope (which is why it has a separate section here), where the electron gun is placed at the bottom. The electron beam goes upwards through three demagnification condenser lenses or, cheaper variant, with a detector inside the SEM/TEM microscope (so-called STEM-in-SEM/TEM). The cheaper solution in the SEM microscope is used at a much lower voltage, around 30 kV. In some cases, it can be argued that STEM replaces a cheaper variant of the TEM microscope. STEM detectors in an SEM microscope are standard of two types:

- *scintillator-light pipe detector* is a relatively expensive detector where the passed electrons are converted into photons using a scintillator, passes through a light-pipe and the end is amplified by a photomultiplier;
- *solid-state detector* is a semiconductor detector – a silicon diode that generates electron-hole pairs directly from transmitted electrons, where this charge is collected.

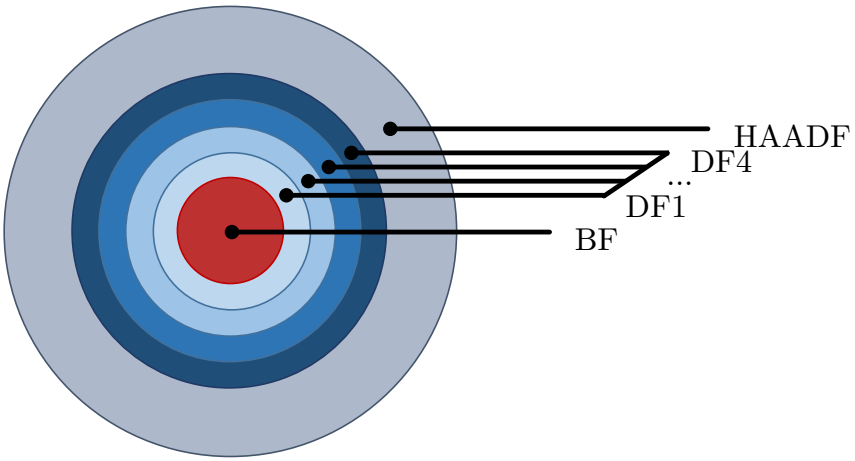

Fig. 1.7: STEM detector and its imaging modes – BF, DF1, DF2, DF3, DF4, and HAADF. The modes are selected according to the deflection of the transmitted electrons from the sample [17].

1.4.4 X-ray photoelectron spectroscopy (XPS)

The XPS method can be used for qualitative, quantitative, and structural analysis. By using X-rays with high energy, the internal electrons of atoms are emitted. By excited electrons with binding energies of 0 to 1500 eV, which are characteristic for each element, it is possible to determine the presence of elements in any mixture uniquely. There is almost no overlap of the lines of the individual elements here.

X-rays hit the sample, from which electrons are released by reason of an external photoelectric effect. By measuring their kinetic energies, it is possible to obtain information about the chemical composition of the surface. Because the electrons are very easily absorbed by the air, it is necessary to perform the measurement in a very high vacuum in the order of 10^{-7} to 10^{-8} Pa.

Electrons are emitted only from a thin surface layer of the sample. Quantitative analysis can be performed under constant determination conditions by evaluating the height or area of the resulting peak.

For the structural analysis, it is possible to use the fact that the internal electron orbitals close to the valence orbitals are partially affected by the formation of a chemical bond – chemical shifts occur.

The correlation of chemical shifts with the change in charge can determine the oxidation number of an atom and determine the change in polarity of bonds.

When studying organic compounds using XPS, shifts induced by the attachment of different functional groups to a given carbon atom can also be observed.

The basic components are the source of primary radiation and the energy analyzer. X-ray source used is most often equipped with two X-ray tube anodes – Mg and Al. These anodes are bombarded by electrons with energies between 10 to

15 kV and emit intense lines K and energies of 1253.6 eV with a half-width of 0.7 eV for Mg and 1486.6 eV with a half-width of 0.85 eV for Al. XPS spectrometers also use synchrotron radiation produced by specially built synchrotrons. This radiation is continuous and very intense, allowing monochromators to use, hence work with continuously tuned photon energy. Energy analyzers work as energy filters, where electrons move in an electrostatic field and only electrons of a given energy pass through the system.

Due to the loss of electrons, the samples charge slightly, which manifests itself as an energy shift in the electron spectrum. The shift must then be corrected according to the known position of a known significant peak. By default, the spectrum is aligned according to the carbon C1s region and the $C - C$ component at 284.8 eV, which occurs in most samples [18].

1.4.5 Raman spectroscopy

Raman spectroscopy is a method of molecular spectroscopy. It uses the interaction of electromagnetic radiation with the sample to monitor rotational and vibrational transitions in the sample molecules.

Raman scattering

It is a phenomenon arising from the interaction between photons of incident light with atoms when energy is transferred to the vibrational and rotational states of atoms or molecules. When photons interact with molecules, elastic or inelastic scattering can occur. We denote elastic scattering as Rayleigh scattering. There is no energy exchange between the photon and the molecule during this process [19]. Inelastic scattering, referred to as Raman scattering, is much less likely (about $10^{-7}\times$) than elastic scattering and involves the exchange of energy between a photon and a molecule, as already mentioned [20].

Inelastic scattering can take place by two mechanisms if the system is initially in the ground state, the photon is excited by the absorption of the photon, and during subsequent deexcitation, the system reaches a state with higher energy than corresponds to the ground state, i. e. the emitted photon has lower energy. This phenomenon is called Stokes scattering. The opposite arises when the excited system is already in a higher energy state at the beginning and reaches the ground state after deexcitation [20]. We refer to this process as anti-Stokes scattering, and the emitted photon has an energy higher than that corresponds by the laser used. Said process is illustrated in Fig. 1.8.

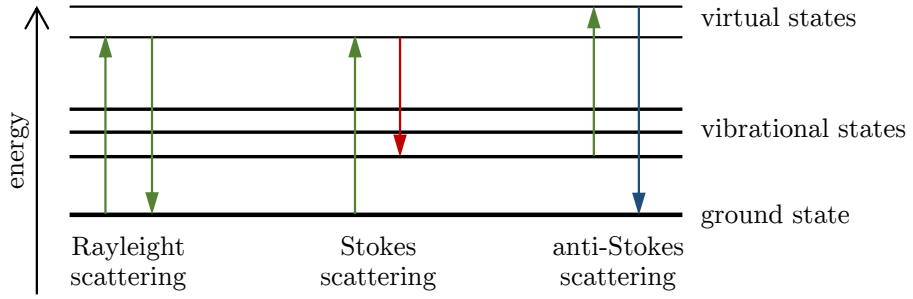

Fig. 1.8: The energy level diagram showing the different processes and the states.

Raman spectroscopy is a complementary method to infrared spectroscopy. Its sensitivity is lower than in infrared spectroscopy. It is more suitable for the observation of non-polar bonds and allows us to observe vibrations even at lower wavelengths, i. e. below 400 cm^{-1}. It allows easy measurement of aqueous solutions because the water provides a weak signal. For the bond vibration to be active in Raman spectroscopy, the polarizability must change during it. If the molecule has a centre of symmetry, the individual vibrations can be active in either infrared or Raman spectroscopy, but not both [21].

1.4.6 Fourier-transform infrared spectroscopy (FTIR)

Infrared spectroscopy is an analytical technique designed primarily for the identification and structural characterization of organic compounds and also for the determination of inorganic substances. It measures the absorption of infrared radiation of different wavelengths by the analysed material. Infrared radiation (IR) is electromagnetic radiation in the wavelength range 12 800 to 10 cm^{-1}. The whole area can be divided into the near (12 800 to 4000 cm^{-1}), middle (4000 to 200 cm^{-1}) and far-infrared area (200 to 10 cm^{-1}), while the most used is the middle area.

The principle of the method is the absorption of infrared radiation as it passages through the sample, during which there are changes in the rotational and vibrational energy states of the molecule depending on changes in the molecule's dipole moment. The analytical output is the infrared spectrum, which is a graphical representation of the functional dependence of energy, usually expressed as a percentage of transmittance (T) or units of absorbance (A) at the wavelength of the incident radiation [22].

Infrared spectroscopy has been used to identify the chemical structure of substances since the 1930s. However, spectrometers operating on the principle of light decomposition (dispersion spectrometers) did not allow the analysis of strongly absorbing matrices. The study of solid samples was mostly limited to powder materials, measured in the form of a mixture with alkali metal halides compressed into thin

tablets, or by capillary layer, suspension of the powder in light aliphatic oil between windows of alkali metal or alkaline earth metal halide windows. Liquid and gaseous samples could be measured in principle without restriction. With the development of computer technology in the 1980s, infrared spectrometers with Fourier transform (FTIR spectrometers) have become a practical expansion. These are instruments working on the principle of spectrum interference, which, unlike dispersive instruments, measure the interferogram of the modulated beam of radiation after passing through the sample [23].

These spectrometers have several advantages, such as high luminosity, high resolution, wavelength accuracy of the obtained spectrum, high recording speed, and the ability to measure in a wide wavelength range. To improve the signal-to-noise ratio, spectra are accumulated in FTIR spectrometers by multiple recordings. The quality data obtained in this way (in digital form) can be further processed, evaluated, and interpreted using computer technology [24].

The spectrometer collects and processes infrared wavelength absorption or spectrum transmissions. Spectra are created when a molecule converts infrared radiation into molecular vibrations. These vibrational movements create bands in the spectrum that occur at specific wavelengths. Each wavelength depends on questions that can be used to determine what types of bonds are present in the sample [25].

1.4.7 Contact angle measurement

The most critical characteristic factor influencing interfacial interactions, such as adsorption, wetting, and adhesion, is surface free (interfacial) energy. Using the contact angle measurement method, differently formed polymers can be easily examined. The contact angle measurement is performed on different inert materials, using a drop shape analysis using a computer and a surface energy evaluation system. The results of measuring contact angles, achieved using various methods of evaluating free surface energy and their outputs, are compared.

This method eliminates the manual way of measuring the contact angle and the experimental error caused by the subjective approach of the operator. A color CCD camera displays the sessile drop. The system is equipped with special software, which controls all necessary operations to calculate the free surface energy. The captured images are displayed in a program that allows immediate matching of the profile of the drop and the arc. The software creates and calculates the angle formed by the substrate of the drop and the tangent of the arc at the point of intersection with this substrate as illustrated in Fig. 1.9. Based on the records of continuous measurement, it is possible to demonstrate the time evaluation of the contact angle [26].

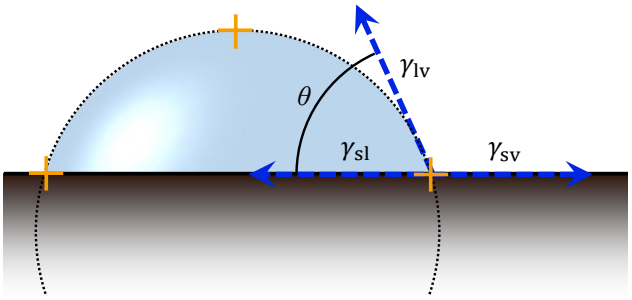

Fig. 1.9: Schematic showing a liquid drop with quantities in the Young equation.

When a drop of fluid is in contact with a flat solid surface, a final contact angle is formed, and the shape of the drop depends on the relative magnitudes of the molecular forces that exist inside the liquid (cohesive) and between the liquid and the solid surface (adhesive). Thus, the magnitude of the contact angle is determined by the liquid and solid's opposing tendencies degree, deciding whether the droplet spreads over the solid surface or is formed by rounding to minimize its area. For example, when a liquid with low surface energy wetting a solid surface gives a zero contact angle, the adhesion of the molecules between the solid surface and the liquid is greater than the cohesion between the water molecules. Conversely, high surface tension liquids form a clearly defined (non-zero) contact angle, indicating that the cohesive force is greater than the liquid and the solid adhesion energy. Young derived the best-known description of the wetting state. Young's equation describes the balance between surface tension at a three-phase interface – liquid phase, solid phase, and gas or vapor phase:

$$\gamma_{sv} - \gamma_{sl} = \gamma_{lv} \cdot \cos\theta, \tag{1.1}$$

where γ_{sv} is the free solid-vapor interfacial energy, γ_{sl} is the free solid-liquid interfacial energy, and γ_{lv} is the liquid-vapor interfacial energy (surface tension). This phases are also illustrated in Fig. 1.9. Liquids for measuring contact angles must meet the following conditions:

- They have high purity.
- They are non-toxic.
- They must not react with the tested surface.
- They have a well-defined and stable free surface energy and its parameters.
- The surface energy of the test liquids must be higher than the energy of the test surface.

The drop profile can be analyzed by two different methods (interpolation and approximation). Fast analysis of the drop profile uses only three measurement points; two must be at the liquid-solid interface to define the baseline, and one should be at the contour of the drop to form the side contour of the drop. The circular radius and contact angle are calculated based on the tangential slope [26].

Several important test parameters can affect the measurement: liquid density, surface quality, temperature, droplet volume, surface pretreatment, drip rate, droplet environment, equilibration time, liquid evaporation, gas adsorption and absorption, partially soluble surfaces, etc. To obtain reproducible contact angles, it is essential to define and adhere to standard conditions. The drop should be as small as possible to eliminate gravity.

The equilibrium time of the contact angle depends on the properties of the liquid, especially on its viscosity. If the angle is measured too early, the value obtained is systematically higher than that in equilibrium. If the angle is measured too late after placement, the value may be affected by evaporation.

Experimental errors that affect the measurement of contact angles are divided into the following groups:

Random errors , i.e., fluctuations of the measured value. The extent of these random errors is determined by the level of accuracy of the measurement. Random errors are often caused mainly by the following cases:

- Inaccurate profile fitting.
- Improper drop placement.
- Inhomogeneity of the sample surface.

Systematic errors occur as a systematic increase or decrease in measured values. They are challenging to detect and can significantly affect the measurement. They can be caused by:

- Drop size.
- Contamination of liquids.
- Reaction of the liquid with a sample of material.
- By measuring the drop before thermodynamic equilibrium is established, or after the drop changes its shape due to evaporation, etc.

2 Materials and methods

The content of this chapter is a description of the parameters of all methods used in the thesis and the devices that provide these methods. The aim is to inform the reader of the exact procedure of specific measurement and production of PVDF nanofibers.

2.1 Production of PVDF nanofibers

Electrostatic spinning is a complex process where countless parameters can influence the properties of the fiber during production, and it is a crucial phase. It is enough to change a single parameter, and the PVDF nanofiber can have a different shape and give fundamentally different electrical characteristics. For this reason, a large part of the work is devoted to the description of the spinning device.

Nanofibers from 20 % PVDF 275 DMSO/AC were manufactured with the Contripro 4SPIN instrument described in Fig. 2.1. The 4SPIN device is used to prepare nanofiber layers from solutions of synthetic or natural polymers and other materials. It is a highly modular device. By combining different types of collectors and emitters, it is possible to create both large-area samples (sheets) with a random structure and samples with a precisely mono- or multi-axially arranged internal structure. By the 4SPIN device, nanomaterials can be created by electrospinning, electroblowing, and electrospraying methods. It is possible to process all common synthetic and natural polymers used for the production of nanofibers. Besides this, the arrangement of the fiber layers can be influenced, and regular 3D fiber structures can be created.

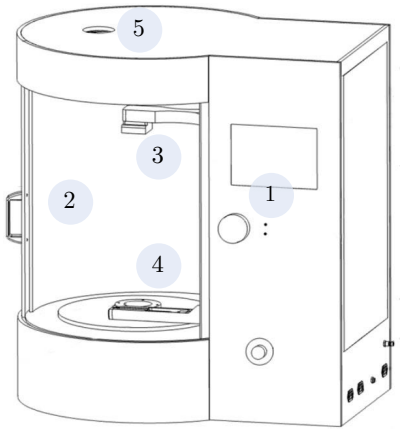

Fig. 2.1: The basic scheme of the electrospinning device: **1)** control panel with touch screen and round element for complete control and setting of the process; **2)** transparent plexiglass separates the spinning chamber with a sliding cylindrical door, where the electrostatic spinning process takes place; **3)** a movable collector arm on which various extensions can be mounted; **4)** a connector for the emitter and an optional air connection, next to which there is also a dosing mechanism and a place for a syringe(s) from which the solution leads through a tube to the emitter; **5)** chamber ventilation.

In addition to various combinations of collectors and emitters, the device also allows the setting of many other parameters. This is, for example, the value of the high voltage on the collector (0 to 60 kV); solution dosing (from 10 µl/min); linear displacement of the collector from the emitter (5 to 25 cm); the collector speed (if a rotary collector is placed) up to 5000 rpm; possibility to use airflow from the emitter at 3 to 99 l/min; air heating 30 to 80 °C. The thickness of the layer of the material itself depends on the emitter used, the area on which the solution is applied, the dosage of the solution, and the application time.

Individual types of emitters can be combined with any type of collector. The non-interchangeability of the collecting and spinning electrodes (emitters and collectors) is ensured by a mechanical way, i.e., by a different kind of clamping mechanism. A single nozzle (with or without air), a multi-nozzle (6 needles), a needle-free nozzle (with or without air), a composite dual nozzle for applying two types of solutions, a composite needle-free dual nozzle, a single coaxial nozzle, and many next. Fig. 2.2 illustrates several examples.

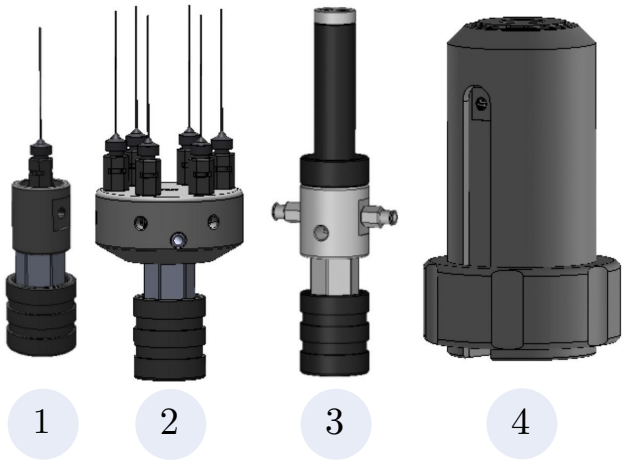

Fig. 2.2: Examples of emitter electrodes of the 4SPIN device: **1)** single nozzle without air; **2)** multi-nozzle; **3)** composite needle-free nozzle; **4)** needle-free multi-nozzle with air.

As the collecting electrode, i.e., the collector, it is possible to use, for example, a static continuous or divided plate, a rotating divided or continuous cylinder, a thin disk, and others. These collectors are illustrated in Fig. 2.3.

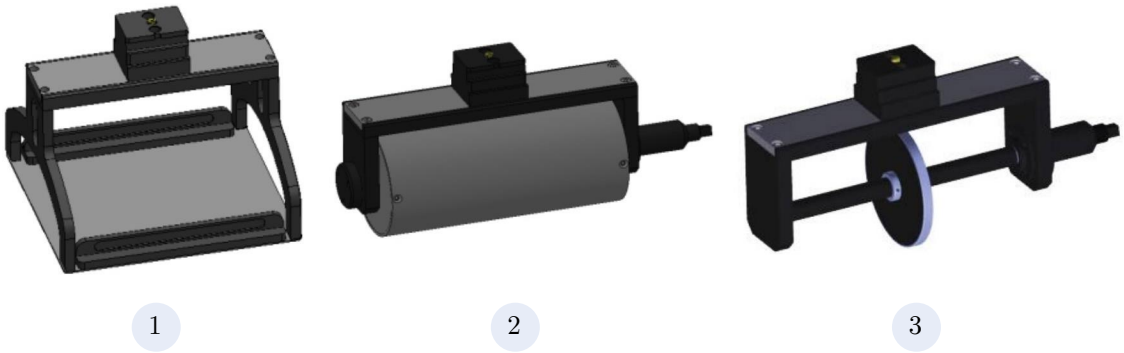

Fig. 2.3: Some selected types of collectors of the 4SPIN device, on which the solution is applied. At **1)** you can see a static continuous surface, at **2)** a continuous rotating cylinder, and at **3)** a thin disk.

After selecting the ideal type emitter and collector comes the choice of parameters. These need to be chosen carefully due to the final shape of the fibers and their properties. For the purpose of this work, only the collector speeds were changed. The resulting spinning with this device can be seen in the illustration in Fig. 2.4.

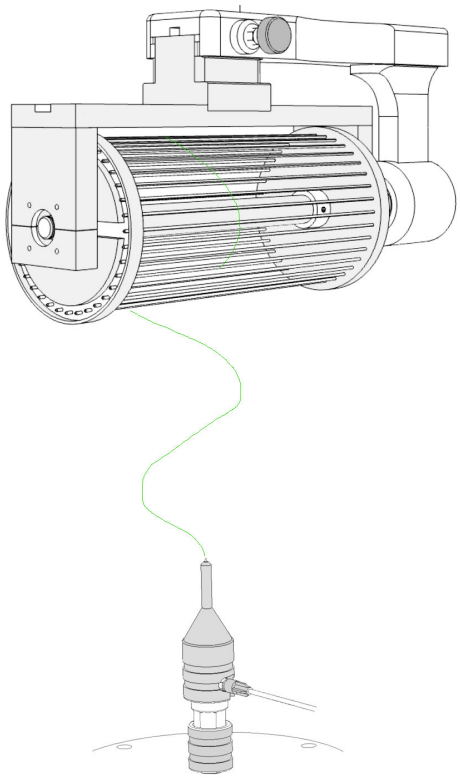

Fig. 2.4: Illustration of electrostatic spinning using the single nozzle using air (cover) as the emitter and the continual cylinder as the collector. The applied fiber is highlighted in green here (the actual color of the fiber depends on the fillers used - for example, the addition of carbon nanotubes is a dark black fiber, the addition of bismuth ferrite is a red fiber). In this work, a continuous cylinder and a single nozzle emitter without air were used.

To eliminate many variables that can interfere with the final products and affect the overall properties of the fiber, parameters and settings have been chosen that create the ideal fiber. A continuous rotating cylinder was selected as the collector. The reason for this choice is that controlling a rotating cylinder speed can be a relatively well-determined thickness and thereby fiber beta phase. The fiber is wound on the cylinder and tensioned according to the speed at which the roller rotates. The fiber on the cylinder is also straightened, so it is directed in one way by default.

On the contrary, the non-directed fibers are chaotically distributed over the collector. The fiber was produced at two different speeds, 300 rpm, and 2000 rpm. These are crucial parameters on which this work will compare fibers. The voltage on the collector was set at 10 kV and was 20 cm away from the emitter. In this work, one needle without air and heating was chosen as the emitter. The nozzle diameter was 17 GA. The reason for this choice is again to remove all variables that could interfere with the resulting measurements. Thanks to the choice of the single nozzle, spinning parameters, such as the thickness of the applied material, the control of fiber formation, and the like, can be controlled relatively precisely.

The disadvantage of this option is the much longer application time, for example, for multi-nozzles or needle-free emitters. However, since work is based mainly on a nanoscale measurement and in many cases only the study of one fiber, this disadvantage becomes negligible. The formation of PVDF fiber from the nozzle and Taylor cone in this work is shown in Fig. 2.5. The solution flow was determined to be 18 µl min^{-1}). The complete parameters are summarized in Tab. 2.1.

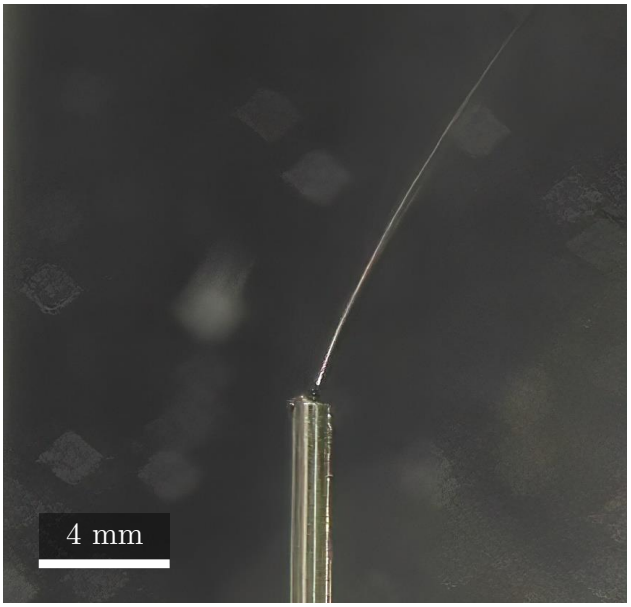

Fig. 2.5: Detail of the nozzle during electrospinning is described in this work. A Taylor cone is formed, and an electrically charged stream of polymer solution is excited. During the flight phase of the solution, which is referred to as the whipping instability, the polymer gradually expands enormously and a nanofiber is formed.

Tab. 2.1: An overview of the basic parameters under which the fibers were spun.

Emitter	**Nozzle size**	**Flow**	**Syringe volume**	**Collector voltage**	**Distance**
Single nozzle	17 GA	18 µl/min	10 ml	50 kV	20 cm

Cylinder speed	**Substrate**	**Temperature**	**Humidity**	**Solution temperature**
300 rpm and 2000 rpm	Aluminum	24 °C	26 %	60 °C

2.2 Morphology and piezoelectric properties

Atomic force microscope with piezoresponse force microscopy mode (NTEGRA Prima microscope) with a tungsten coated tip and bias voltage of −5 to 5 V was used as characterization method for investigation of morphology and piezoelectric

domains. The gold surface was used as a contact for characterization of PVDF-fibers by electrical modes.

The samples were prepared by electrospinning method on the firm gold-coated silicon substrates with square dimension of 10×10 mm. The results after fabrication at collector speed of 300 and 2000 rpm were compared. The area measured by microscope had dimensions of 10×10 µm. The measurements were performed in several sites and several times in a row to confirm the results. Only one fiber was characterized at a time. Visualization is performed in both two-dimensional and three-dimensional view. Scan velocity was from 8.04 to 13.94 µm/s

2.3 Wettability of a solid surface

The See System by Advex Instruments – a computer-based instrument with a mechanical table and a camera for sensing a drop of liquid on the measured sample was used to measure the contact angle and wettability of the samples. The sample was cut in the form of a thin strip on which 10 drops of demineralized water were gradually applied. The measurement is affected by significant deviations due to random and systematic errors. Therefore, it is advisable to measure the sample in several places and several times to eliminate these errors. Each drop of water had a volume of exactly 3 µm. After applying the drop to the sample, 5 s were allowed to stabilize. This exact time was measured thanks to the continuous imaging of the computer application by the camera. After this time, the contact angle of the drop was recorded. This measurement was performed 10× for one type of sample. All results were averaged and entered into the table, including errors. From the standard deviation of the mean, an absolute error was listed with the Student's t-distribution $t_{\mathrm{np}} = 2.32$ for a probability of 95 %. The results were classified as either hydrophilic <90°, hydrophobic >90°, highly hydrophobic >120°, or superhydrophobic >150°.

2.4 Internal and external structure of the fiber

Specific parameters of PVDF fibers were observed by scanning electron microscopes (SEM). The first – SEM microscope with STEM detector – FEI Helios NanoLab 660, monitored the fiber composition using a high-angle annular dark-field imaging detector. The accelerating voltage was set to 30 kV and the current 50 pA, which is a sufficient value for electrons that pass through the polymer fiber.

The second – microscope with a focused ion beam (FIB) was the Tescan Lyra3. Here, the fibers were not observed longitudinally, as in the previous case, but as a cross-section. The accelerating voltage was set to 5 kV for SEM observation. When

cutting, the FIB high voltage was 30 kV, and for precise fiber separation, the current was only 50 pA. This is a small value for cutting, as the fiber had to be cut very finely to avoid defects. A thin layer of 20 nm thick carbon was also coated before observing due to fiber fixation and preventing charge accumulation.

It is important to emphasize that the fibers were not coated for this purpose, as they were observed longitudinally, and the sputtered area could affect the observation. For this reason, it was necessary to make high-speed image accumulations. The fibers were placed on a gold grid here, and the observations took place very close to the conductive parts to allow the charge to dissipate. Only in this way was it possible to achieve relatively good image quality even though the fiber was not coated. The gold grid was placed during electrospinning production on the same sheet on the cylinder collector so that all studied samples have identical parameters.

2.5 Elemental fingerprint and chemical composition

Raman spectroscope (WITec alpha300 R) was used to monitor the phase formation described in Section 1.2. A green laser with a wavelength of 532 nm with a power of 5 mW was used. The spectrum was accumulated 30× with an integration time of 7 s. The magnification of the lens was set to 100×. Due to the thickness of the laser beam incident on the sample's surface, a single fiber is not possible to characterize. The diameter of the fibers ranges from tens of nanometers to units of microns. The fibers should not be stressed during measurement with high laser power and long irradiation time. Otherwise, they may degrade and thus change the resulting spectra. Due to the inhomogeneous surface of the sample, the measurement was performed in several sites and several times in a row. The uneven surface and the characteristic shape of the fibers also affected the overall reflection of light and thus reduced the total signal intensity.

Transmission experiment was performed by Fourier infrared spectrometer Vertex80v, also for phase investigations [27]. The spectral range 4000 to 400 cm^{-1} was measured. From this range, area of interest was selected. The measurement took place in a vacuum chamber. A pre-measured background was subtracted from the resulting spectra, and a baseline correction was performed.

Observations of the structure and electrical properties were also supplemented by AXIS Supra Kratos X-ray photoelectron spectroscop to determine the fiber's elemental composition and its chemical states. Wide spectra and high-resolution bands were measured. The emission current of 15 mA and X-ray power of 225 W were the same for both types of measurements. The binding energy of the wide spectrum was measured in the range of 1200 to 0 eV.

3 Experimental results

The results obtained from measurements using several methods mentioned in Sec. 1.4 and 2 are described below. These are measurements by electron microscopy, including transmission observation with a STEM detector and observation of the fiber in cross-section by FIB. Spectral analysis was performed by Raman spectroscopy, FTIR, and XPS. The wettability and contact angle of water were also measured on the samples. The produced PVDF nanofibers are characterized both in terms of material and structural, as well as in terms of elemental composition. Most measurements were performed on two different types of samples – at different collector speeds of 300 and 2000 rpm [28].

From the results below, several findings affecting the material properties are evident. In Fig. 3.1 and 3.5, nanofibers are observed by SEM imaging with clearly different thicknesses. It can be seen from Fig. 3.1 that at different collector speeds, the arrangement and shape of the nanofibers is very different. Thus, a higher collector speed causes thinning of the fibers [27]. These differences affect the outcome of piezoelectric behaviour. Interestingly, in Fig. 3.1b fiber diameters are relatively similar compared to Fig. 3.1a where fibers vary from 452 nm to 2.2 µm.

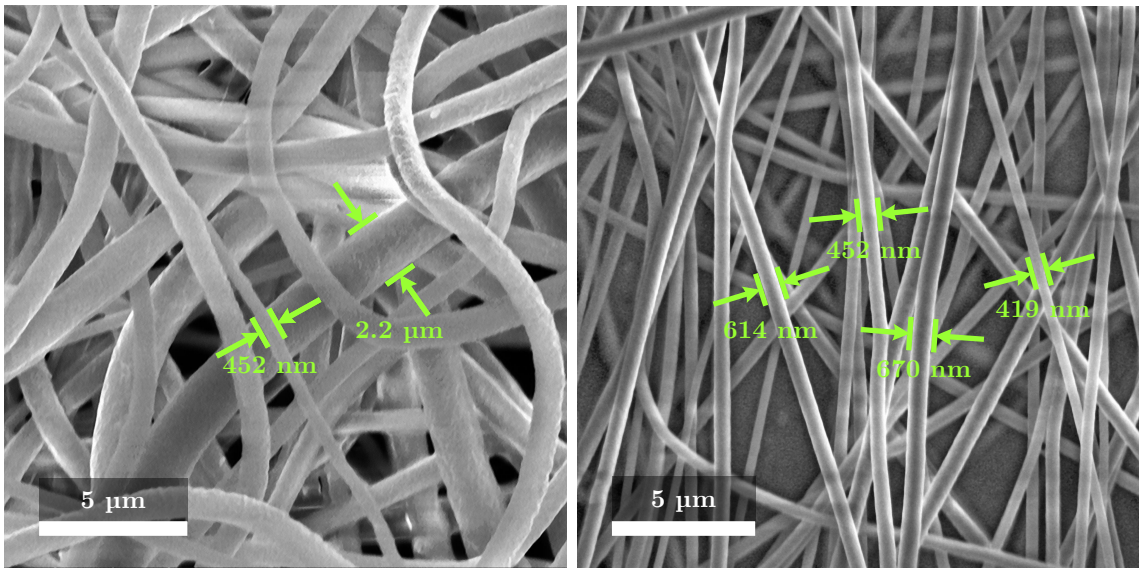

a) b)

Fig. 3.1: SEM image of PVDF fibers prepared at **a)** 300 rpm and **b)** 2000 rpm collector speed. The differences in fabrication are particularly noticeable in the arrangement and thickness of the fibers.

Chaotic and uniformly oriented fiber alignment can then have a significant effect on many material properties. On closer examination, I focused directly on the

characterization of one fiber by SEM microscopy, as I describe in Fig. 3.2. Since the fibers exhibit considerable movement when irradiated with the electron beam and there is charging and the low possibility of observation, it was necessary to perform a coating. For example, gold or platinum can be used as the coating material. However, carbon was fully sufficient for this purpose. Standard thicknesses for observing non-conductive materials with an electron microscope are about 10 nm or less. In my case, however, it was necessary to use thicker layers with a value of 20 nm, since, despite the 10 nm layer, there was still mobility of nanofibers, which means a relatively high electroactivity.

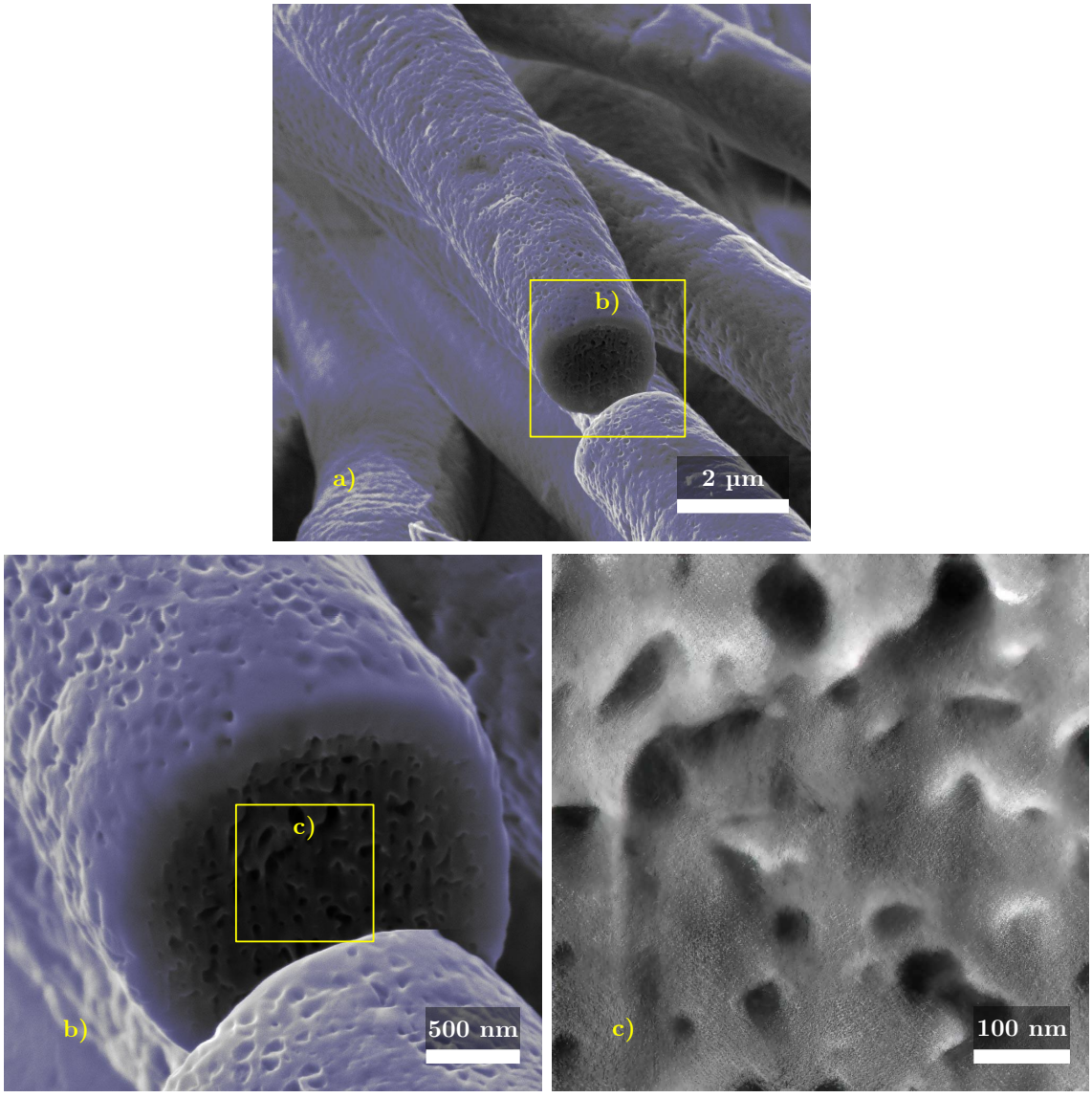

Fig. 3.2: Detail of PVDF nanofiber in cross-section and its porous structure after fabrication with 300 rpm of collector speed. All three figures describe the same fiber structure, gradually focusing from **a)** the largest to **c)** the most significant detail.

The gradual view field, where a yellow rectangle bounds the magnification area in Fig. 3.2, captures the nanofiber down to the most significant detail. Fig. 3.2a shows some of the fibers I focused on. I chose one of them and very finely cut by the FIB and with a current of 50 pA. The melting point of polyvinylidene fluoride is 177 °C, but even much lower temperatures already affect its structure. Such a precise cut allowed no melting by beam and other deformation to occur, as seen in Fig. 3.2b. Deformation of the fiber would distort the complete results, and the final image would not be beneficial. Figures 3.2a and 3.2b also show colored parts. These colored parts represent carbon, i.e., a thin protective layer, thanks to which the fiber was coated and fixed against movement. It was colored by violet from the differentiation and better orientation for the reader from the original PVDF material. Carbon coating is, therefore, not an original part of nanofibers. In figure 3.2c there is no coating, as can be seen. This is the focus of the fiber core itself, where a porous structure is visible. Such pores reach a diameter of about 5 nm to 50 nm, and their occurrence is in almost every fiber. Thus, it can be assumed that the strength of the fiber is directly affected by this porous structure and its other properties.

Another very interesting phenomenon is shown in Fig. 3.3, where again the fiber's cross-section is performed similarly as in the previous case with a current of 50 pA. In the same way, it is distinguished here by the purple color carbon coating, which is applied only for the needs of observation under an electron microscope. The yellow rectangles are centered on the cross-section of the fibers, which are shown in Fig. 3.3b and in Fig. 3.3c. In both cases, there is a large gap inside the fiber. It can also be said about Fig. 3.3b that the fiber is hollow inside. Particularly around this fiber core, the porosity no longer occurs as in the previous case in Fig. 3.2. The occurrence of smaller holes/pores is rather along the edges [29].

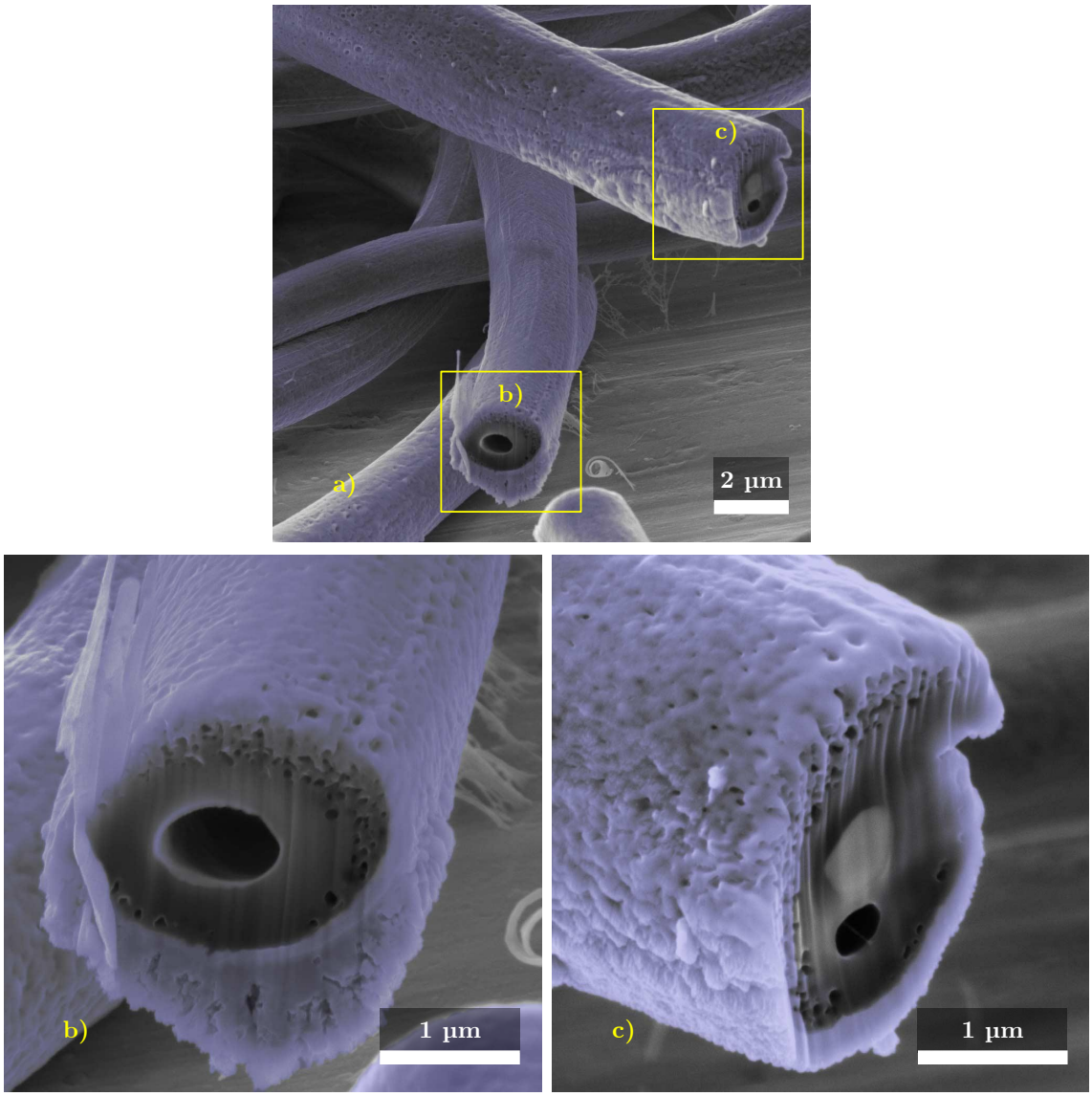

Fig. 3.3: Two fibers in a cross-sectional view and their hollow structure after fabrication with 2000 rpm of collector speed.. The two fibers together are shown in figure **a)** and their detail in figure **b)** and **c)**. Their structure is slightly different from previous figure 3.2.

Figure 3.4a shows the fiber produced at 300 rpm and Fig. 3.4b at 2000 rpm. The purplish tone of the fiber highlights a different structure that needs to be emphasized. In addition to the variety in different fiber thickness, which is different at first glance, the fiber structure affects not only the strength but also the piezoelectric properties. Interesting are defective spherical shape structures that occur over almost the entire width of the fiber in Fig. 3.4b. The origin of these shapes is unknown and may be caused, for example, by a collector speed, a dosing rate, or a solution concentration [30]. This phenomenon opens up further possibilities for research and testing of defects depending on manufacturing parameters.

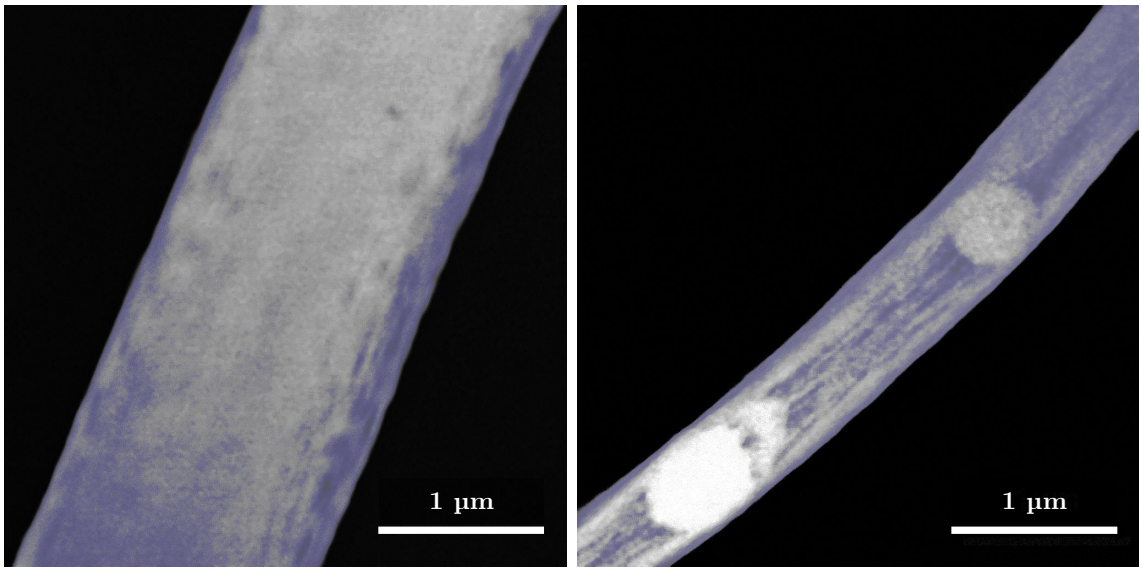

a) b)

Fig. 3.4: Internal fiber structure at collector drum speeds **a)** 300 rpm and **b)** 2000 rpm observed by STEM and HAADF method.

The latest electron microscope observation focuses on different nanofiber thicknesses for different spin speeds in detail. The individual fibers in Fig. 3.5 are seen with greater view field. There is also a different porosity visible in the cross-section of these fibers. Higher porosity predominates in the fiber in Fig. 3.5a with pore size up to 500 nm in diameter [31]. On the contrary, the pores already mentioned for the fiber in Fig. 3.5b are complicated to distinguish. It is also worth mentioning that the individual fibers are not always spun into a circular shape, as shown in Fig. 3.5b, which certainly affects both the piezo effect and the tensile strength. The needle and dose rate used can have a significant impact on such a fiber shape.

In previous cases, Tescan Lyra3 was used for observation and cross-section. But in Fig. 3.5 different scanning electron microscope (FEI Helios NanoLab 660) with an acceleration voltage of electron beam of 5 kV and current 1.6 nA was used for observation of nanofibers arrangement and FIB at 30 kV and 2.5 nA for cross-section investigating of individual fibers. These values mean that for the FIB the current was 50× higher than for the cross-section in Fig. 3.2, or in Fig. 3.3. So, it is necessary to pay attention to cutting, when the fibers begin to deform and what effect this may have. A good alternative is the use of a cryogenic chamber, where the sample would be cooled to a very low temperature and would not have to be deformed during cross-section.

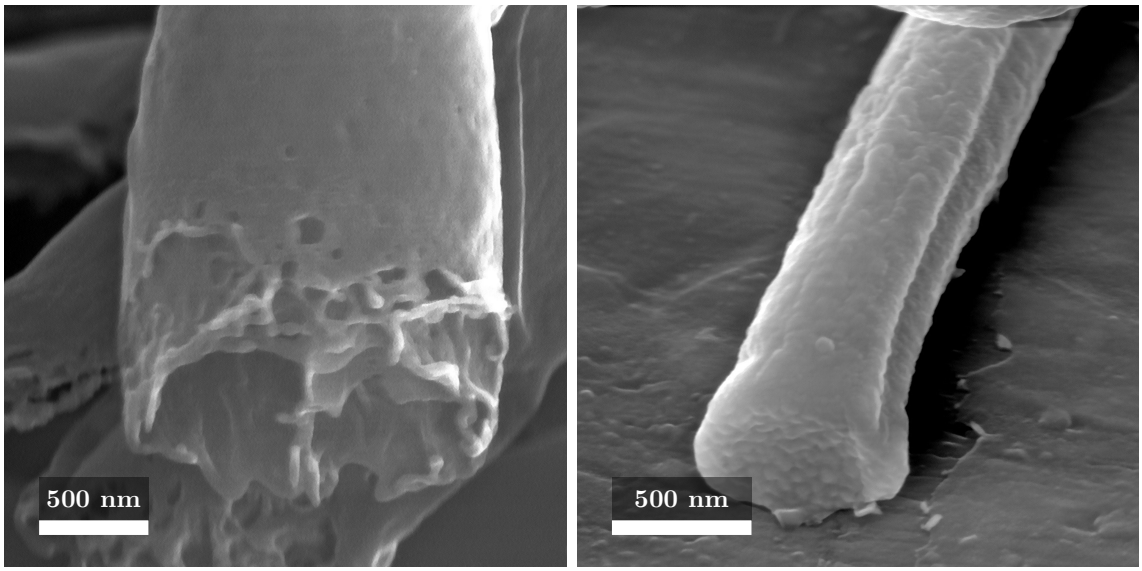

a) b)

Fig. 3.5: Individual fibers of PVDF material. Fiber **a)** with 300 rpm fabrication collector speed shows an increased porosity compared to fiber **b)** with 2000 rpm fabrication collector speed, where the pores are almost noticeable.

The defective rounded structure of the fiber obtained in Fig. 3.5b by SEM was also scanned using AFM for the cases of both collector speeds in Fig. 3.6. Morphology is captured in both three-dimensional and two-dimensional representations. It was confirmed that fibers of imperfect shapes form at both speeds of 300 rpm (Fig. 3.6a) and speeds of 2000 rpm (Fig. 3.6b).

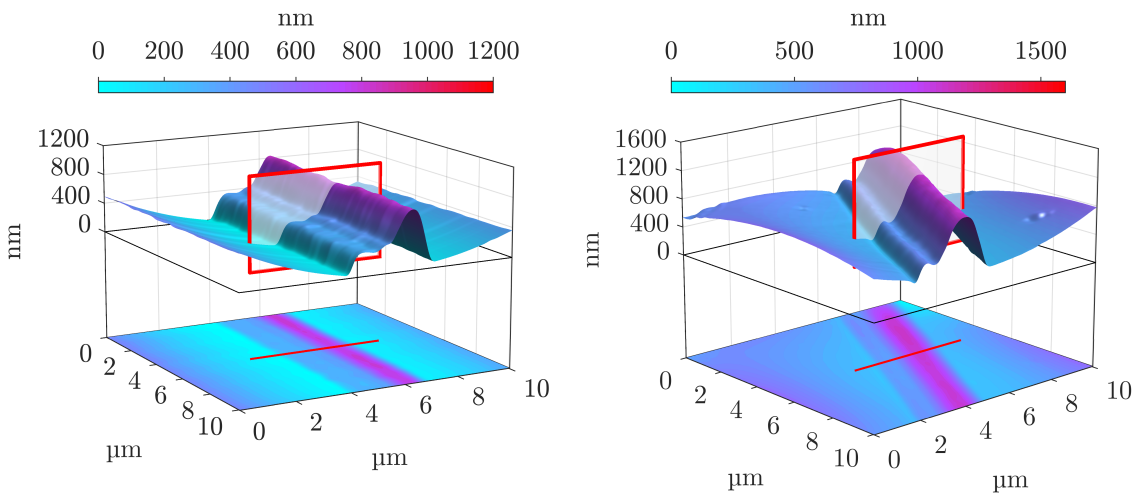

a) b)

Fig. 3.6: Morphological structure of PVDF nanofibers scanned by AFM with different collector speeds (300 rpm in **a)** and 2000 rpm in **b)**).

As a post-processing method, a cross-section was created using Matlab. Microscope data were extracted and processed. As shown in Fig. 3.6, red rectangles were drawn across each fiber in the three-dimensional graph and lines in the two-dimensional graph. These marks indicate a cut similar to that made by the FIB in Figs. 3.2 and 3.3. Of course, in this case, it is a software cut, which means that no formations can be seen in the fiber's core. However, this method is handy if we need to know the exact morphology, more precisely, the profile of the fibers [32]. Since AFM has a much higher resolution than SEM, which was used in this work (better resolution can be achieved only with a TEM microscope), the possibility of obtaining very useful morphological information is achieved. In Fig. 3.7 we see, as already indicated, that the profile has a relatively similar shape in both cases of the electrospinning speed. It is also important to note the different ratio of x and y axes, which is intentionally different for fiber shape specifications. It can be stated that the shape of these fibers is not directly affected by the speed of the collector cylinder. On the contrary, it affects the thickness of the fibers, which has already been mentioned and is clearly evident from Fig. 3.4 or Fig. 3.5 [33].

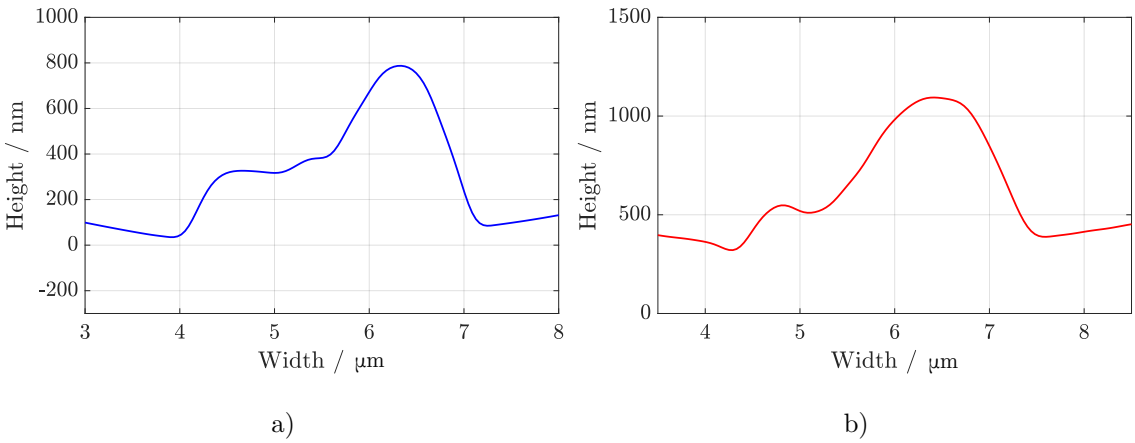

Fig. 3.7: Software sample cross-section from AFM with different collector speeds (300 rpm in **a)** and 2000 rpm in **b)**).

Identical fiber measured by AFM microscope was also measured by PFM method. The piezoelectric response of the fiber were confirmed. This was used for the fiber with a more decisive β phase – at the collector cylinder speed of 2000 rpm (Fig. 3.6b). The change in polarization is most visible along the edges of the fiber, described in Fig. 3.8. Here, the color of these edges changes from light green to deep red in the form of a thin line. The voltage was varied from -5 to 5 V. I verified that the shape of the fiber has a direct effect on its electrical properties and behavior. On the edges of the fiber, which was observed from its morphology in the previous Fig. 3.6b, you can see dipole changes due to the adjustment of bias voltage from -5

to 5 V. These dipole changes are significantly affected by hysteresis when returning to 0 V. From this point of view, it can be stated that nanofibers are functional with the piezoelectric response, but they are affected by its shape [34, 28].

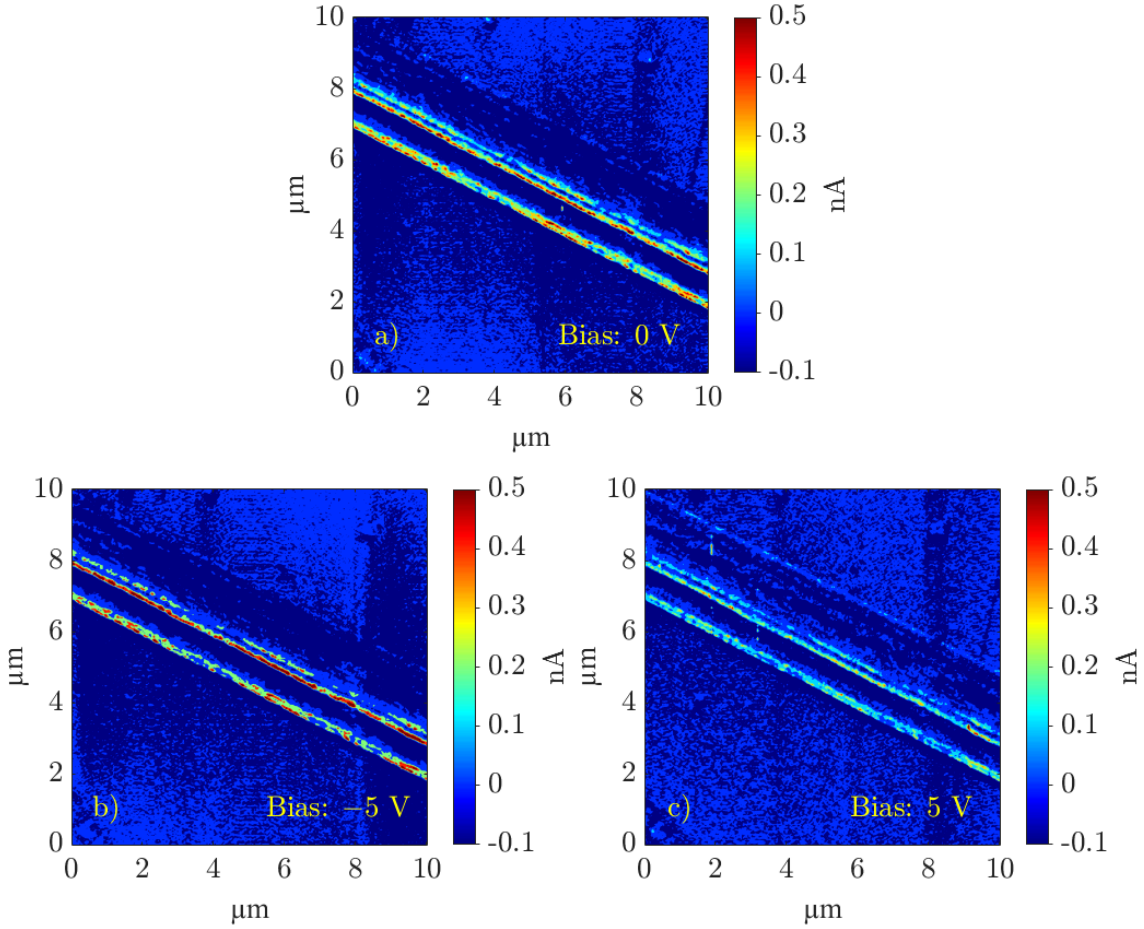

Fig. 3.8: Piezoelectric response of PVDF nanofiber with the imperfect circular shape at biasing of **a)** 0 V, **b)** −5 V, and **c)** 5 V.

Another measurement using piezoresponse force microscopy monitors the exact morphology (Fig. 3.9a) of the fiber and its electrical parameters (Fig. 3.9b), which vary mainly along its perimeter up to 1 nA. In this case the presence of electrostatic interaction should be taken into account. By this reason, it is possible to follow only qualitative difference of the fibers appearance after applying large voltages. The response of vertically oriented domains is observed in Mag-signal [2].

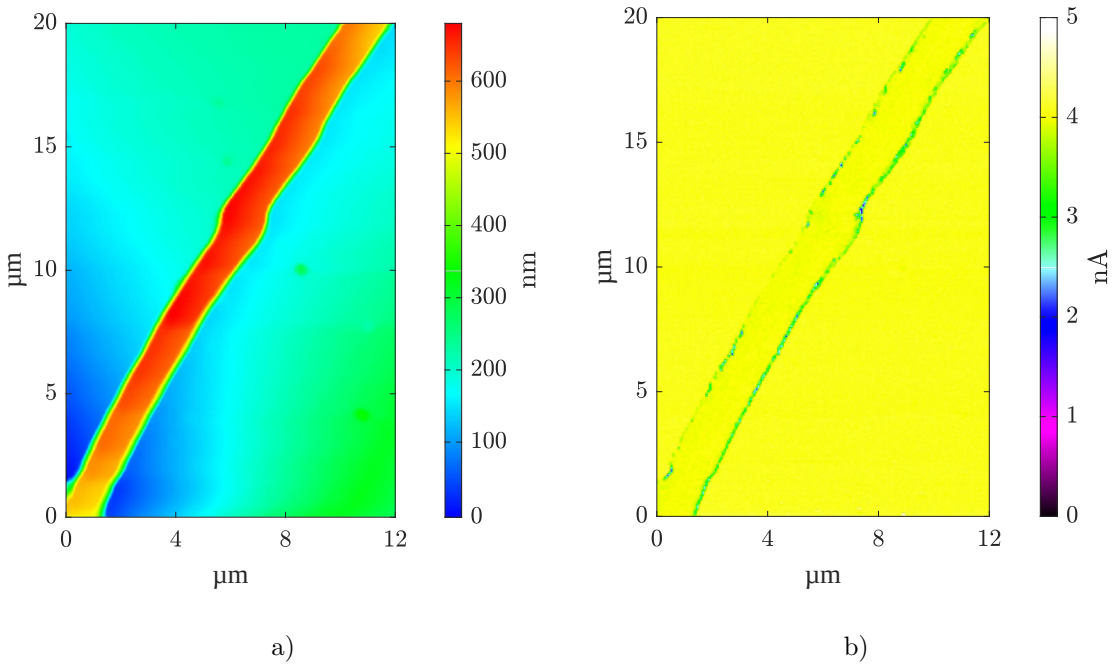

Fig. 3.9: Measured **a)** morphology and **b)** electrical response of vertically oriented domains of single fiber by PFM method.

Typical Raman spectra of PVDF material in Fig. 3.10 describes a molecular parameters in the range of 150 cm^{-1} to 3150 cm^{-1}. Attention was focused on the spectrum in the range of 760 cm^{-1} to 880 cm^{-1}, where α and β phase peaks are illustrated in detail and differences in their ratio are measured [35]. The differences in ratio on the two different types of samples are less noticeable in Raman spectroscopy, and therefore FTIR was used for a more precise comparison of the β phase [36].

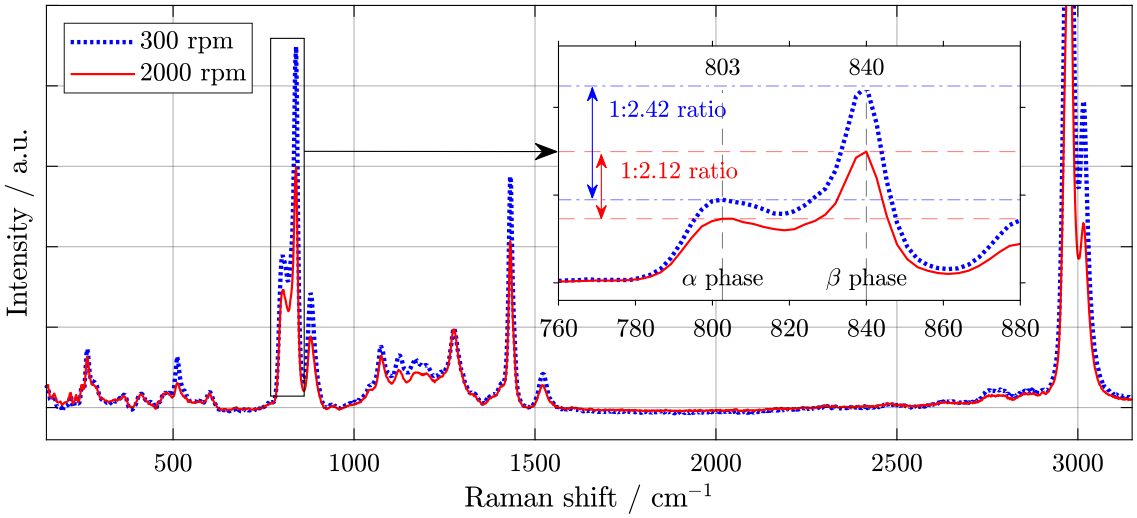

Fig. 3.10: Nanofibers PVDF material investigated using a Raman spectroscopy with focus to 760 cm^{-1} to 880 cm^{-1} region.

Spectra of FTIR in Fig. 3.11 shows dependence of the transmittance on the wavelength of the whole sample between 1500 cm^{-1} to 400 cm^{-1}. The β phase is strongly visible at 840 cm^{-1} [37]. It is evident that the β phase is higher for fibers produced at the collector speed of 2000 rpm than for fibers produced at a collector speed of 300 rpm. So, it can be concluded that the piezoelectric effect will show higher values for the fibers at the collector speed of 2000 rpm. These samples will be given special attention to piezoelectric measurements by PFM [38].

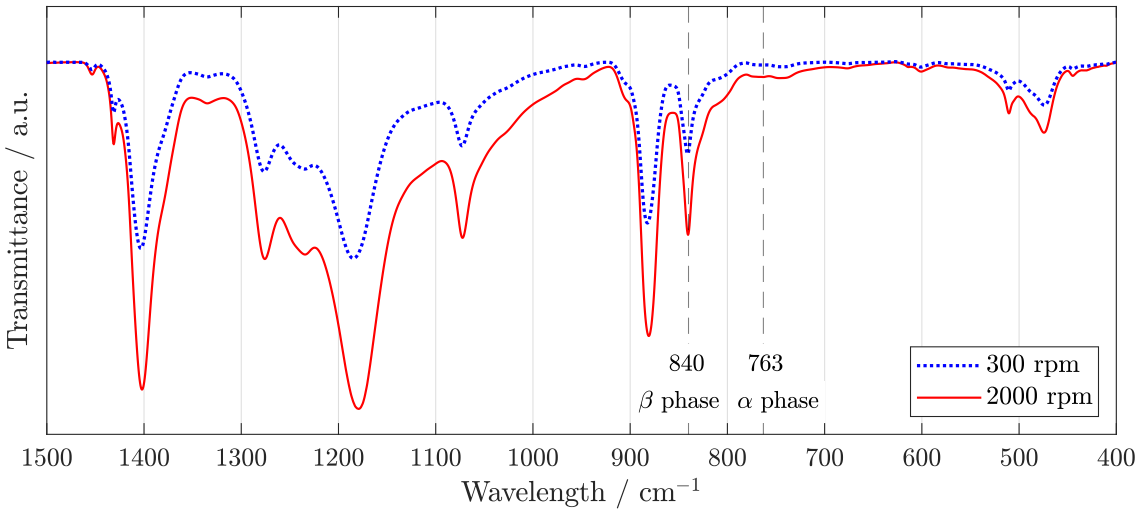

Fig. 3.11: FTIR transmittance spectrum of PVDF nanofiber sample with 300 rpm and 2000 rpm collector speed. Emerging phases α and β are indicated by a dashed line.

The surface chemistry of a material to a depth of 10 nm was examined by measuring the kinetic energy of electrons using XPS. From the survey spectrum of PVDF polymer and wide energy range, we can see several significant peaks, which indicate the presence of several important elements in Fig. 3.12. As we already know from the chain conformations of Fig. 1.1, PVDF consists mainly of hydrogen H, fluorine F, and carbon C. Its chemical formula is $-(C_2H_2F_2)_n-$. It is essential to mention that hydrogen is very difficult to trace from XPS, as it has no core electrons. Hydrogen contains only one valence electron, and therefore it isn't easy to detect it with the X-ray diffraction method. For example, the neutron diffraction method is more beneficial for hydrogen detection, but I did not deal with it in this work. However, oxygen can also be detected on the material's surface. Oxygen is found in almost every surface exposed to the atmosphere. Thus, in Fig. 3.12, peaks carrying important information are indicated by a gray stripe. The peaks in the region of C1s, O1s, and F1s, i.e., core-level emissions, are significant. The figure shows samples made at both 300 rpm and 2000 rpm.

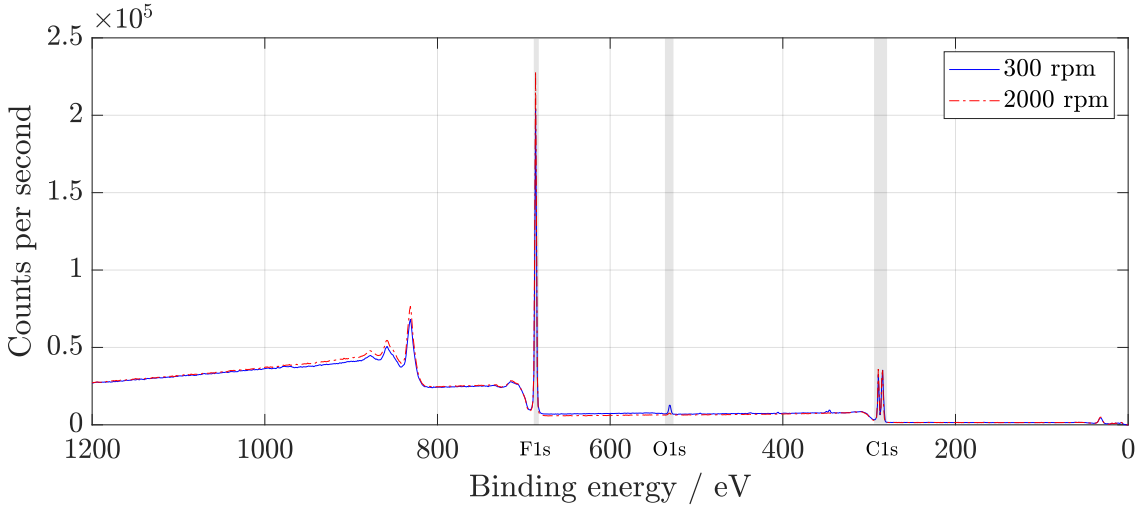

Fig. 3.12: Comparison of two XPS wide spectra of PVDF nanofiber sample with 300 rpm and 2000 rpm collector speed.

One of the most crucial spectrum can be considered the carbon region. In addition to the sample components, it can also be adventitious carbon contamination, therefore, similarly to oxygen, it can occur more or less in many samples. However, in my case, the presence of carbon in the sample is desirable, as was written above. In the C1s region, there are several critical binding energies of chemical states that are characteristic for PVDF. A typical carbon fingerprint of PVDF is evident in Fig. 3.13. Occurring bonds are CF_2 (gray), $FC-OH$ (purple), $C-O$ (green), $C-O/CH_2$ (blue), and $C-C/C-H$ red. Since they cannot be directly identified from the measured spectrum, which delimits the bonds by the black line, it was necessary to use fitting, i.e., post-processing after the measurement, and to model them mathematically. From these results, concrete bonds can already be successfully determined [39]. In the sample in Fig. 3.13b, a change in the ratios of the $FC-OH$ and $C-O/CH_2$ bonds is observed, as well as a slight increase. On the contrary, a significant decrease occurred for $C-C/C-H$ [40].

Minimal changes in Fig. 3.14 are observed for fluorine. These changes are mainly due to minor differences between semi-ionic and covalent bonds, which means an insignificant crystalline phase shift. For a sample produced at 2000 rpm, this shift is then observable from the increase in binding energy.

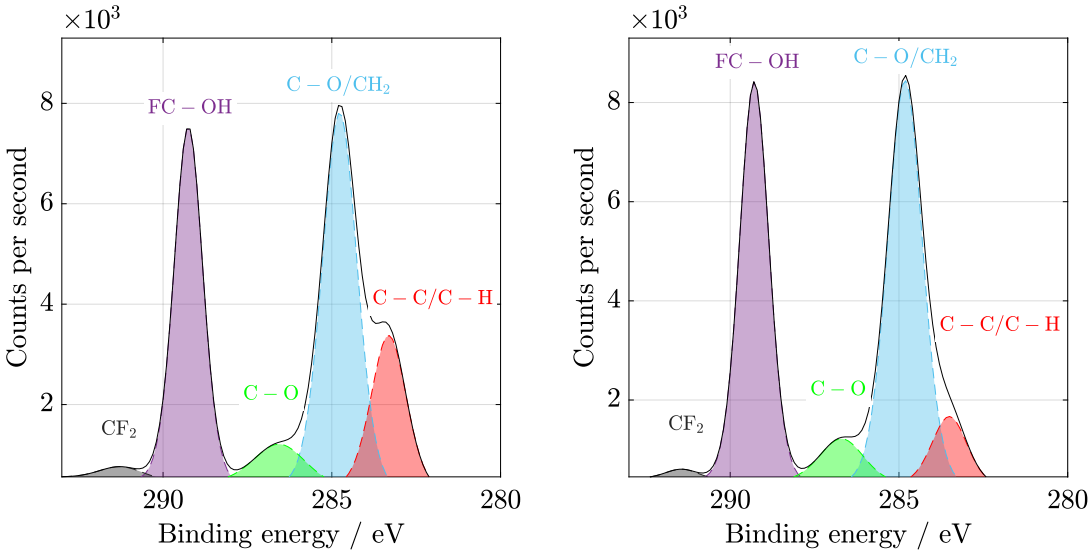

Fig. 3.13: XPS spectra represented the C1s high-resolution energy band's expressed by an envelope, fitted and divided into individual peaks of certain bonds in the material [41]. A more substantial $C-C/C-H$ binding (red peak) is recognised on the fiber produced at **a)** 300 rpm compared to the fiber produced at **b)** 2000 rpm.

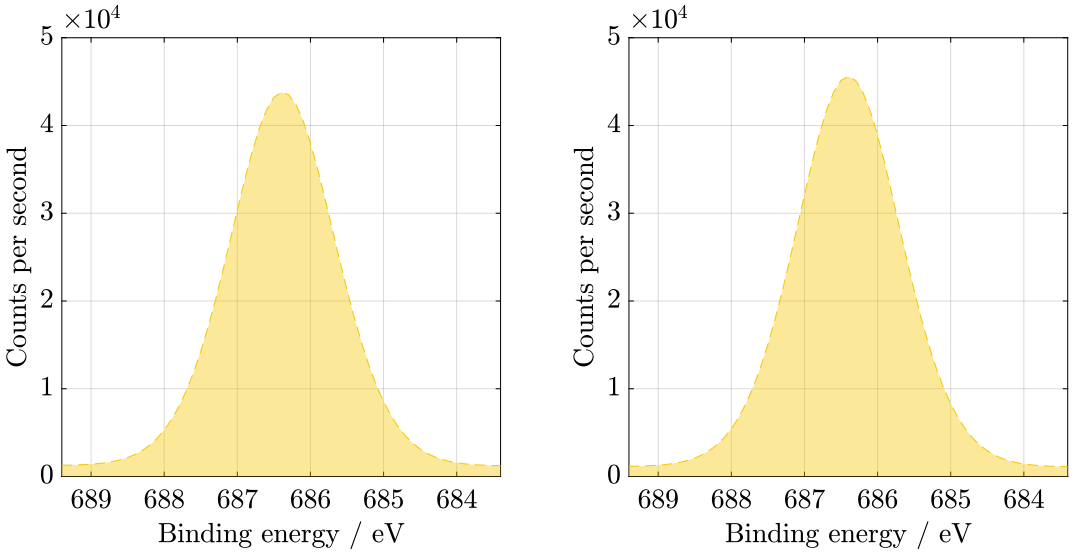

Fig. 3.14: High-resolution energy band of F1s orbital electron. The differences between two differently spun samples are relatively minimal for the fluorine.

From the O1s region in Fig. 3.15, oxygen can be recognized. Oxygen was introduced into the PVDF during production, where PVDF was exposed to air. In most cases, this region is composed of peaks with oxygen bounds to carbon and hydrogen. Due to the minimal occurrence, which can be compared in relation to the other regions in Fig. 3.12, the binding energy for the O1s region is very small. For this reason, the actual measured value without fitting (which is colored in purple) was also marked in figure with a black line. In other cases, nevertheless, the measured spectra are very detailed and accurate. Figure 3.15b shows a significant decrease in the oxygen bound to PVDF produced at a higher rate of 2000 rpm [42].

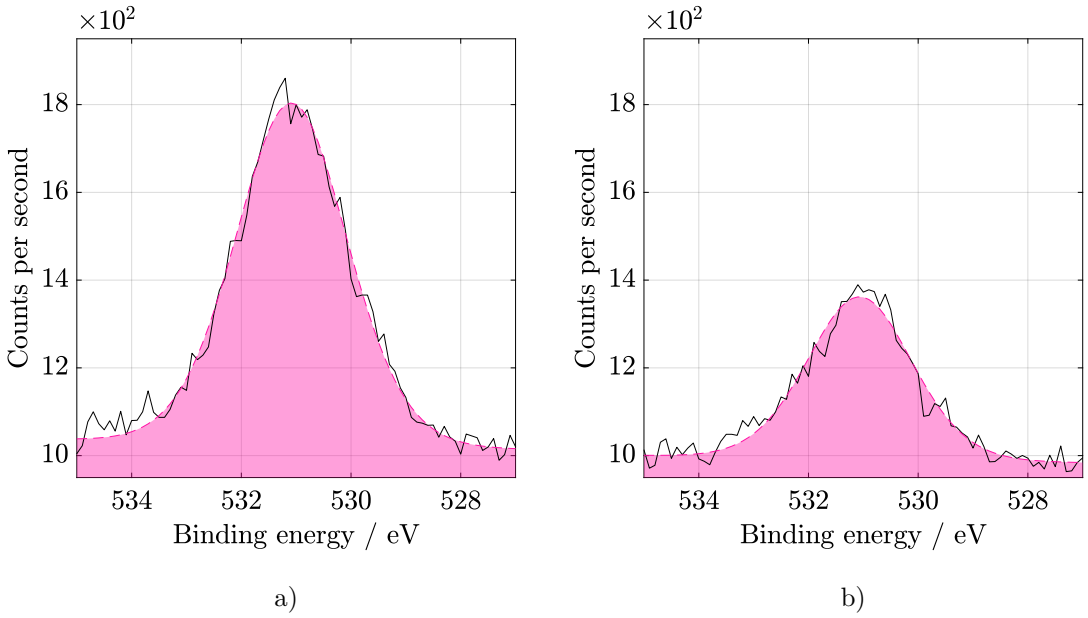

Fig. 3.15: High-resolution energy band of O1s orbital electron.

Evaluation of hydrophobicity and hydrophilicity by measuring the contact angle of the drop of demineralized water on the surface of the sample of PVDF nanofibers at two different collector drum speeds showed significant differences. Figure 3.16 shows two drops of water. Each applied to a differently made specimen. The contours of the water drops are marked by a yellow line, as well as the interface between the sample and another environment. The contact angle gripping the water drop with the sample in the form of blue arrows is also drawn in the photos for better orientation [43].

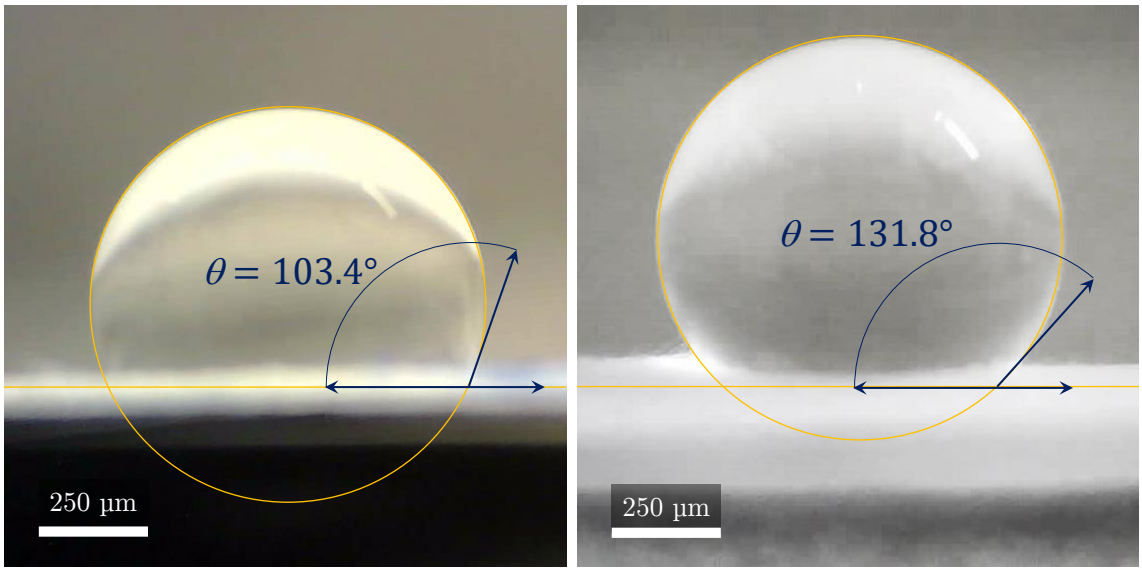

a) b)

Fig. 3.16: Hydrophobicity and hydrophilicity measurement. The figures show two 3 µl droplets and specimens and their different wettability. Figure **a)** shows a more wetted sample with a hydrophobic surface. Hence, the same hydrophobic to the almost superhydrophobic surface has the sample in figure **b)** with fibers arranged in parallel.

It is clear from Fig. 3.16a that the mechanical balance of the drop is entirely different from the mechanical balance of the drop in Fig. 3.16b, where the specimen is spun at 2000 rpm. Table 3.1 also evaluates all measurements that were averaged and from which the contact angle of the drop was determined. The sample in Fig. 3.16b achieves much less wettability, i.e., greater hydrophobicity, due to the parallel arrangement of the fibers [44]. Conversely, in Fig. 3.16a, where the fibers are chaotically arranged, the hydrophobicity is lower. Samples where the fibers are chaotically arranged as well as the fibers arranged in parallel at higher speeds can be considered hydrophobic. Since in both cases, the contact angle of 90° determining the hydrophobicity of the material was exceeded. The material in Fig. 3.16b is then approaching superhydrophobicity (contact angle of 150°) [45].

Tab. 3.1: Measured contact angles for two different samples. For higher accuracy, ten measurements were performed, and the results were averaged and measurement errors calculated.

	Measurement number	1	2	3	4	5	6	7	8	9	10	Mean	Error
Contact angle / °	300 rpm	108.8	113.5	107.8	101.1	98.2	98.9	99.4	106.8	95.7	104.1	**103.4**	4,2
	2000 rpm	135.8	138.1	126.2	130.5	131.0	129.0	129.2	135.5	128.5	134.5	**131.8**	2,9

Conclusion

In this work, I successfully created polymeric PVDF nanofibers exhibiting piezoelectric properties. The fibers were produced by electrospinning in two types – at the collector cylinder speed of 300 rpm and 2000 rpm. These collector speeds greatly affected their resulting behavior and parameters.

Structural, molecular and electrical properties of PVDF nanofibers at different collector speed were measured. The resulting findings show that after fabrication at 300 rpm collector speed, the structure is composed of non-uniform electrospun fibers. Also, the diameter and orientation of these observed nanofibers are not completely uniform and have higher porosity unlike fibers with fabrication at 2000 rpm collector speed, which are more uniform. However, the uniformity of nanofibers can be achieved by many other changes, for example, by increasing the amount of polymer flow in electrospinning, leading to more interactions between polymer chains in solution [12].

According to FTIR and Raman spectroscopy was evaluated the phase composition where all α, β and γ are present. Raman spectroscopy provides information from the surface and near-surface area. Whereas FTIR spectra were collected in transmission mode at the samples of tens microns. According to calculations from FTIR, the thinner fibers has larger amount of β phase [46]. For the PFM, the response of vertically oriented domains is observed mainly on the edges of the fiber where a variation of current occurs. The fiber can exhibit edges and other imperfect shapes without the addition of any powders and other fillers, as verified by morphological examination using AFM.

Quite remarkable results were achieved in the measurement of hydrophobicity and hydrophilicity, where it was found that the speed of the collector cylinder significantly affects the wettability of the resulting material.

The results of this characterization of PVDF nanofibers contribute in a relatively new scope in the form of better fabrication processes of this promising material. This unexplored area in the nanoscale opens up new possibilities for other future researches.

There are considerable opportunities to expand the work. Many of them are based on the PVDF applications, such as wearable electronics, smart textiles or filters. However, to achieve the best possible β phase, it is necessary to research and tune other parameters of nanofibers in their production. So what fibers will have properties depends from the beginning where their production starts. The quality of the fibers itself also affect the piezoelectric parameters. Which is one of their most important properties, where their whole use then comes from, and where efforts need to be targeted.

References

1. ZHANG, John X.J.; HOSHINO, Kazunori. Implantable Sensors. In: *Molecular Sensors and Nanodevices*. Elsevier, 2014, pp. 415–465. Available from DOI: 10.1016/b978-1-4557-7631-3.00007-7.
2. SOIN, N.; ANAND, S.C.; SHAH, T.H. Energy harvesting and storage textiles. In: *Handbook of Technical Textiles*. Elsevier, 2016, pp. 357–396. Available from DOI: 10.1016/b978-1-78242-465-9.00012-4.
3. ČÁSTKOVÁ, Klára et al. Structure–Properties Relationship of Electrospun PVDF Fibers. *Nanomaterials*. 2020, vol. 10, no. 6, p. 1221. ISSN 2079-4991. Available from DOI: 10.3390/nano10061221.
4. HE, Weidong et al. Self-supporting smart air filters based on PZT/PVDF electrospun nanofiber composite membrane. *Chemical Engineering Journal*. 2021, vol. 423, p. 130247. ISSN 13858947. Available from DOI: 10.1016/j.cej.2021.130247.
5. PISARENKO, Tatiana. Characterization of PVDF nanofibers created by the electrospinning method. In: *Proceedings of the 26th Conference STUDENT EEICT 2020*. Brno, 2020, pp. 287–291. ISSN 978-80-214-5735-5.
6. SASMAL, Abhishek; SEN, Shrabanee; DEVI, Parukuttyamma Sujatha. Synthesis and characterization of SmFeO3 and its effect on the electrical and energy storage properties of PVDF. *Materials Research Bulletin*. 2020, vol. 130, p. 110941. ISSN 00255408. Available from DOI: 10.1016/j.materresbull.2020.110941.
7. XIN, Yi et al. Full-fiber piezoelectric sensor by straight PVDF/nanoclay nanofibers. *Materials Letters*. 2016, vol. 164, pp. 136–139. ISSN 18734979. Available from DOI: 10.1016/j.matlet.2015.09.117.
8. PISARENKO, Tatiana. PVDF — an ideal candidate for use in nanogenerators. In: *Proceedings of the 27th Conference STUDENT EEICT 2021*. Brno, 2020.
9. SENGUPTA, D. et al. Characterization of single polyvinylidene fluoride (PVDF) nanofiber for flow sensing applications. *AIP Advances*. 2017, vol. 7, no. 10, p. 105205. ISSN 21583226. Available from DOI: 10.1063/1.4994968.
10. VOIGTLÄNDER, Bert. *Scanning Probe Microscopy*. Berlin, Heidelberg: Springer Berlin Heidelberg, 2015. NanoScience and Technology. ISBN 978-3-662-45239-4. Available from DOI: 10.1007/978-3-662-45240-0.
11. XIN, Yi et al. A brief review on piezoelectric PVDF nanofibers prepared by electrospinning. *Ferroelectrics*. 2018, vol. 526, no. 1, pp. 140–151. ISSN 15635112. Available from DOI: 10.1080/00150193.2018.1456304.

12. SUKIGARA, Sachiko et al. Regeneration of Bombyx mori silk by electrospinning - Part 1: Processing parameters and geometric properties. *Polymer*. 2003, vol. 44, no. 19, pp. 5721–5727. ISSN 00323861. Available from DOI: 10.1016/S0032-3861(03)00532-9.

13. ASLAN, Enes et al. The Electrospinning Process. In: *Virtual Prototyping & Bio Manufacturing in Medical Applications*. Springer International Publishing, 2021, pp. 153–185. Available from DOI: 10.1007/978-3-030-35880-8_7.

14. CHENG, Chen et al. Controlled nanofibers morphology and its influence on magnetic properties by electrospinning. *Applied Physics A: Materials Science and Processing*. 2020, vol. 126, no. 11, pp. 1–5. ISSN 14320630. Available from DOI: 10.1007/s00339-020-04010-6.

15. KHOLKIN, A.L.; KISELEV, D.A.; HEREDIA, A. Piezoresponse Force Microscopy. In: *Encyclopedia of Materials: Science and Technology*. Elsevier, 2011, pp. 1–8. Available from DOI: 10.1016/b978-0-08-043152-9.02281-8.

16. RUIZ-CASTELL, Pedro. Scanning electron microscopy. In: *Between Making and Knowing*. World Scientific, 2020, pp. 503–512. Available from DOI: 10.1142/9789811207631_0044.

17. BROWNING, N. D.; CHISHOLM, M. F.; PENNYCOOK, S. J. Atomic-resolution chemical analysis using a scanning transmission electron microscope. *Nature*. 1993, vol. 366, no. 6451, pp. 143–146. ISSN 00280836. Available from DOI: 10.1038/366143a0.

18. PAPEŽ, Nikola et al. Characterization of GaAs Solar Cells under Supercontinuum Long-Time Illumination. *Materials*. 2021, vol. 14, no. 2, p. 461. ISSN 1996-1944. Available from DOI: 10.3390/ma14020461.

19. TITUS, Deena; JAMES JEBASEELAN SAMUEL, E.; ROOPAN, Selvaraj Mohana. Nanoparticle characterization techniques. In: *Green Synthesis, Characterization and Applications of Nanoparticles*. Elsevier, 2019, pp. 303–319. Available from DOI: 10.1016/b978-0-08-102579-6.00012-5.

20. LE PEVELEN, D. D.; TRANTER, G. E. FT-IR and raman spectroscopies, polymorphism applications. In: *Encyclopedia of Spectroscopy and Spectrometry*. Elsevier, 2016, pp. 750–761. ISBN 9780128032244. Available from DOI: 10.1016/B978-0-12-409547-2.12161-4.

21. MCNALLY, Patrick J.; SATHE, Vasant G. Raman Spectroscopy: Basics and Applications. In: *Nanomaterials*. Weinheim, Germany: Wiley-VCH, 2012, 495 –534. Available from DOI: 10.1002/9783527646821.ch7.

22. DHAND, Vivek et al. Fabrication of robust, ultrathin and light weight, hydrophilic, PVDF-CNT membrane composite for salt rejection. *Composites Part B: Engineering*. 2019, vol. 160, pp. 632–643. ISSN 13598368. Available from DOI: 10.1016/j.compositesb.2018.12.106.

23. BAI, Haolong; WANG, Xuan; ZHOU, Yitong; ZHANG, Liping. Preparation and characterization of poly(vinylidene fluoride) composite membranes blended with nano-crystalline cellulose. *Progress in Natural Science: Materials International*. 2012, vol. 22, no. 3, pp. 250–257. ISSN 10020071. Available from DOI: 10.1016/j.pnsc.2012.04.011.

24. DUTTA, Aastha. Fourier Transform Infrared Spectroscopy. In: *Spectroscopic Methods for Nanomaterials Characterization*. Elsevier, 2017, vol. 2, pp. 73–93. ISBN 9780323461467. ISSN 0006-2960. Available from DOI: 10.1016/B978-0-323-46140-5.00004-2.

25. CAI, Xiaomei; LEI, Tingping; SUN, Daoheng; LIN, Liwei. A critical analysis of the α, β and γ phases in poly(vinylidene fluoride) using FTIR. *RSC Advances*. 2017, vol. 7, no. 25, pp. 15382–15389. ISSN 20462069. Available from DOI: 10.1039/c7ra01267e.

26. BURŠÍKOVÁ, V. et al. *Vyhodnocení povrchové energie materiálu ošetřeného plazmatem, metodou měření kontaktního úhlu*. Brno: Masarykova univerzita, 2004.

27. MOTAMEDI, Asma Sadat et al. Effect of electrospinning parameters on morphological properties of PVDF nanofibrous scaffolds. *Progress in Biomaterials*. 2017, vol. 6, no. 3, pp. 113–123. ISSN 2194-0509. Available from DOI: 10.1007/s40204-017-0071-0.

28. UEBERSCHLAG, Pierre. *Sensor Review*. Vol. 21, PVDF piezoelectric polymer. MCB UP Ltd, 2001. No. 2. ISSN 02602288. Available from DOI: 10.1108/02602280110388315.

29. MANIKANDAN, N. et al. Fabrication of Piezoelectric Polyvinylidene Fluoride (PVDF) Polymer-Based Tactile Sensor Using Electrospinning Method. *Nano Hybrids and Composites*. 2016, vol. 12, pp. 42–50. Available from DOI: 10.4028/www.scientific.net/nhc.12.42.

30. HUANG, H. S. et al. Identification of ionic aggregates in PVDF-g-PSSA membrane by tapping mode AFM and HADDF STEM. *Applied Surface Science*. 2006, vol. 253, no. 5, pp. 2685–2689. ISSN 01694332. Available from DOI: 10.1016/j.apsusc.2006.05.048.

31. MOKHTARI, F.; LATIFI, M.; SHAMSHIRSAZ, M. Electrospinning/electrospray of polyvinylidene fluoride (PVDF): Piezoelectric nanofibers. *Journal of the Textile Institute*. 2016, vol. 107, no. 8, pp. 1037–1055. ISSN 17542340. Available from DOI: 10.1080/00405000.2015.1083300.

32. ARJUN HARI, M.; RAJAN, Lintu; SUBASH, C.K.; VARGHESE, Soney. Effect of nanoparticle size on the piezoelectric properties of PVDF based nanocomposite thin films. *Materials Today: Proceedings*. 2021. ISSN 22147853. Available from DOI: 10.1016/j.matpr.2021.02.715.

33. SOBOLA, Dinara et al. Complementary SEM-AFM of swelling Bi-Fe-O film on HOPG substrate. *Materials*. 2020, vol. 13, no. 10. ISSN 19961944. Available from DOI: 10.3390/ma13102402.

34. SENCADAS, V. et al. Local piezoelectric response of single poly(vinylidene fluoride) electrospun fibers. *physica status solidi (a)*. 2012, vol. 209, no. 12, pp. 2605–2609. ISSN 18626300. Available from DOI: 10.1002/pssa.201228136.

35. KASPAR, Pavel et al. Case Study of Polyvinylidene Fluoride Doping by Carbon Nanotubes. *Materials*. 2021, vol. 14, no. 6, p. 1428. ISSN 1996-1944. Available from DOI: 10.3390/ma14061428.

36. ELASHMAWI, I. S.; GAABOUR, L. H. Raman, morphology and electrical behavior of nanocomposites based on PEO/PVDF with multi-walled carbon nanotubes. *Results in Physics*. 2015, vol. 5, pp. 105–110. ISSN 22113797. Available from DOI: 10.1016/j.rinp.2015.04.005.

37. ISLAM, Atif; KHAN, Ahmad Nawaz; SHAKIR, M. Fayzan; ISLAM, Kashif. Strengthening of β polymorph in PVDF/FLG and PVDF/GO nanocomposites. *Materials Research Express*. 2019, vol. 7, no. 1, p. 015017. ISSN 20531591. Available from DOI: 10.1088/2053-1591/ab5f82.

38. SALIMI, A.; YOUSEFI, A. A. FTIR studies of β-phase crystal formation in stretched PVDF films. *Polymer Testing*. 2003, vol. 22, no. 6, pp. 699–704. ISSN 01429418. Available from DOI: 10.1016/S0142-9418(03)00003-5.

39. KAYNAK, Akif et al. Study of Radio Frequency Plasma Treatment of PVDF Film Using Ar, O2 and (Ar + O2) Gases for Improved Polypyrrole Adhesion. *Materials*. 2013, vol. 6, no. 8, pp. 3482–3493. ISSN 1996-1944. Available from DOI: 10.3390/ma6083482.

40. KASPAR, Pavel et al. Characterization of Polyvinylidene Fluoride (PVDF) Electrospun Fibers Doped by Carbon Flakes. *Polymers*. 2020, vol. 12, no. 12, p. 2766. ISSN 2073-4360. Available from DOI: 10.3390/polym12122766.

41. YAN, Dedao et al. Synergistic modification effect of polyvinylidene fluoride and polydopamine on mechanical and damping properties of three-dimensional braided carbon fibers reinforced composites. *Journal of Materials Science*. 2019, vol. 54, no. 7, pp. 5457–5471. ISSN 15734803. Available from DOI: 10.1007/s10853-018-03223-8.

42. MOHAMMADI GHALENI, Mahdi et al. Fabrication of Janus Membranes for Desalination of Oil-Contaminated Saline Water. *ACS Applied Materials and Interfaces*. 2018, vol. 10, no. 51, pp. 44871–44879. ISSN 19448252. Available from DOI: 10.1021/acsami.8b16621.

43. LIAO, Yuan et al. Fabrication of polyvinylidene fluoride (PVDF) nanofiber membranes by electro-spinning for direct contact membrane distillation. *Journal of Membrane Science*. 2013, vol. 425-426, pp. 30–39. ISSN 03767388. Available from DOI: 10.1016/j.memsci.2012.09.023.

44. HUANG, F. L. et al. Dynamic wettability and contact angles of poly(vinylidene fluoride) nanofiber membranes grafted with acrylic acid. *Express Polymer Letters*. 2010, vol. 4, no. 9, pp. 551–558. ISSN 1788618X. Available from DOI: 10.3144/expresspolymlett.2010.69.

45. KEBEDE, Temesgen Girma; DUBE, Simiso; NINDI, Mathew Muzi. Biopolymer electrospun nanofibres for the adsorption of pharmaceuticals from water systems. *Journal of Environmental Chemical Engineering*. 2019, vol. 7, no. 5, p. 103330. ISSN 22133437. Available from DOI: 10.1016/j.jece.2019.103330.

46. KE, Guizhen; JIN, Xinya; HU, Haoxuan. Electrospun polyvinylidene fluoride/-polyacrylonitrile composite fibers: fabrication and characterization. *Iranian Polymer Journal (English Edition)*. 2020, vol. 29, no. 1, pp. 37–46. ISSN 1735-5265. Available from DOI: 10.1007/s13726-019-00773-9.

List of symbols

Symbol	Description	Unit
A	absorbance	%
d	piezoelectric charge coefficient	C/m
g	piezoelectric voltage coefficient	V m/N
T	transmittance	%
γ_{lv}	surface tension	°
γ_{sl}	free solid-liquid interfacial energy	°
γ_{sv}	free solid-vapor interfacial energy	°
$\tan\delta$	dielectric dissipation factor	–
ε	permittivity or dielectric constant	F/m
θ	contact angle	°

List of acronyms

Acronym	Description
AC	Acetone
AFM	Atomic force microscopy
BF	Bright-field
DF	Dark-field
DMSO	Dimethyl sulfoxide
FfeS	Far-field electrospinning
FIB	Focused ion beam
FTIR	Fourier-transform infrared spectrometry
GFIS	Gas field ion source
HAADF	High-angle annular dark-field
IR	Infrared radiation
LMIS	Liquid metal ion source
NfeS	Near-field electrospinning
PFM	Piezoresponse force microscopy
PVDF	Polyvinylidene fluoride or polyvinylidene difluoride
RPM	Revolutions per minute
SE	Secondary electrons
SEM	Scanning electron microscope
SPM	Scanning probe microscopy
STEM	Scanning transmission electron microscopy
TEM	Transmission electron microscopy

List of units

Unit	Description	Notation
A	electric current	ampere
a.u.	ratio of intensity amount	arbitrary unit
°C	Celsius temperature	degree Celsius
eV	amount of kinetic to move an electron across a electric potential difference of 1 V	electronvolt
GA	diameter of the needle	gauge
l	volume of one cubic decimetre	liter
l/s	volumetric flow	liter per second
m	the base unit of length	meter
m/s	change in velocity or speed per time interval	meter per second
m^{-1}	Raman shift	reciprocal metres
rpm	number of turns in one minute	revolutions per minute
V	voltage, electric pressure, electric tension or electric potential difference	volt
W	1 joule of work performed in 1 second	watt